[American Journal of Science, Vol. 312, May, 2012, P. 534–571, DOI 10.2475/05.2012.03]

LONG-TERM EXHUMATION OF AN AEGEAN METAMORPHIC CORE COMPLEX GRANITOIDS IN THE NORTHERN MENDERES MASSIF, WESTERN TURKEY

ELIZABETH CATLOS*, LAUREN JACOB**, TOLGA OYMAN***, and SORENA SORENSEN§

ABSTRACT. The Eğrigöz, Koyunoba, and Alaçam plutons are located in the northern portion of the Menderes Massif, a region characterized today by large-scale extension. To gain a better understanding of their exhumation history, we acquired zircon ages, geochemical analyses, and cathodoluminescence (CL) images to search for evidence of micro- to macro-scales of deformation. The combination is a powerful means to decipher their tectonomagmatic history. *In situ* ion microprobe $^{238}U/^{206}Pb$ zircon ages of the granitoids range from 30.0 ± 3.9 Ma to 14.7 ± 2.6 Ma (±1σ) and indicate the plutons crystallized over ~15 m.y. The dated zircons show CL zoning consistent with igneous crystallization and are only located adjacent to or as inclusions in biotite grains. The youngest ages are dominated by a blue color in CL, whereas a majority of older zircons are yellow. Higher Th/U contents are typically shown by zircons with black or dark green colors in CL. Most of the samples of these granitoids indicate they are magnesian, calc-alkalic and peraluminous granite to granodiorites, but variations exist, likely reflecting heterogeneity caused by magma mixing, partial melting, crustal contamination, and post-emplacement fluid interactions as evidenced by the CL images. CL images show that all samples experienced magma mixing, multiple episodes of brittle deformation, and fluid-mediated alteration. Sources for the generation of Northern Menderes Massif granitoids include simple slab induced upwelling from the subduction of the African plate along the Hellenic arc, adiabatic decompression as the northern edge of Turkey's Anatolide-Tauride block delaminates, and upwelling asthenosphere as the continental lithosphere thins during extension. We present a model in which western Turkey is an amalgamation of stacked subduction zones that transition from north to south over time. Northern Menderes Massif granitoids document their complex geologic history in their ages, chemistry, and textures.

Key words: Zircon geochronology, cathodoluminescence, Menderes Massif, granitoid, western Turkey, subduction

INTRODUCTION

The Menderes Massif, located in southwest Turkey, is the largest known metamorphic core complex on Earth, covering an area of >40,000 km^2 (Westaway, 2006) (fig. 1). A core complex forms when lithospheric extension accommodated by detachment faults exposes medium- to high-grade metamorphic rocks (Coney, 1980; Coney and Harms, 1984; Lister and Davis, 1989). In many of these systems, including in the Menderes Massif, igneous rocks are cut or deformed by large-scale extensional structures (Hetzel and others, 1995; Keay and others, 2001; Dilek and others, 2009; Catlos and others, 2010; Denele and others, 2011; Howard and others, 2011). Igneous rocks may play an important role in the development of core complexes by thinning and weakening crust and driving isostatic doming (Corti and others, 2003). These

* University of Texas at Austin, Department of Geological Sciences, 1 University Station C1100, Austin, Texas 78712-0254, USA
** Apache Corporation, 2000 Post Oak Boulevard, Suite 100, Houston, Texas 77056-4400, USA
*** Dokuz Eylul University, Faculty of Engineering, Department of Geological Engineering, Tinaztepe-Buca, 35160, Izmir, Turkey
§ Department of Mineral Sciences, Smithsonian Institution, PO Box 37012, MRC 119, Washington, DC 20013-7012
Corresponding author: Elizabeth Catlos. E-mail: ejcatlos@gmail.com

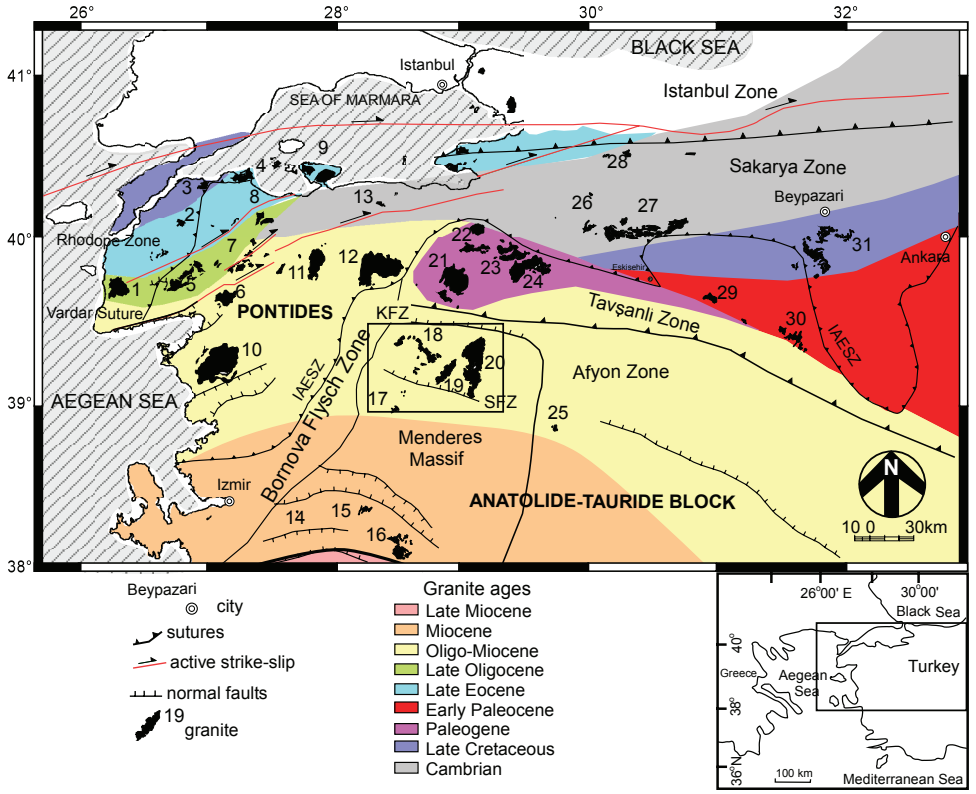

Fig. 1. Map showing major structures and locations of 31 plutons in western Turkey (Delaloye and Bingöl, 2000; Şenel and Aydal, 2002; Okay, 2008). Red lines are approximate locations of active strands of the North Anatolian Fault. Names corresponding to the numbers are (Delaloye and Bingöl, 2000; Boztug and others, 2009, may vary in the literature): 1. Kestanbol, 2. Kuşçayir, 3. Şevketiye, 4. Karabiga, 5. Evciler, 6. Eybek, 7. Yenice, 8. Katrandağ, 9. Kapidağ, 10. Kozak, 11. Ilıca, 12. Çataldağ, 13. Karacabey, 14. Turgutlu, 15. Salihli, 16. Alaşehir, 17. Gördes, 18. Alaçam, 19. Koyunoba, 20. Eğrigöz, 21. Orhaneli, 22. Topuk, 23. Göynükbelen, 24. Tepeldağ, 25. Baklan, 26. Bilecik, 27. Inhisar, 28. Pamukova, 29. Kaymaz, 30. Sivrihisar, 31. Beypazarı. Box outlines the field area in figure 2. KFZ = Kütahya Fault Zone, SFZ = Simav Fault Zone, IAESZ = İzmir-Ankara-Erzincan Suture Zone.

rocks may also time extension by the nature of their relationship with large-scale normal faults (Keay and others, 2001; Ring and Collins, 2005; Howard and others, 2011).

Magma bodies can also drive the formation of back arc basins, of which the Aegean Sea is considered by many to be a classic locality (Agostini and others, 2010). The sources of magma in a back arc setting may be via the melting of the subducting slab, a random mantle plume, or delamination (Flower and others, 2001). Magmas in the Aegean region may migrate and geochemically evolve due to the roll back of the subducting African slab (ten Veen and Postma, 1999; Bonev and Beccaletto, 2007; Dilek and Sandvol, 2009). Here we focus on understanding the timing and geochemical evolution of three granitoid plutons located in the northern Menderes Massif (also called the Gördes Massif) to understand how extension in the Aegean region is recorded by these bodies.

The Eğrigöz (Turkish for "crooked-eye"), Koyunoba, and Alaçam (or Alaçamdağ) granitoids are located in the hanging wall of the Simav normal fault in the northern Menderes Massif (figs. 1 and 2). These plutons are located within a wider NW-SE

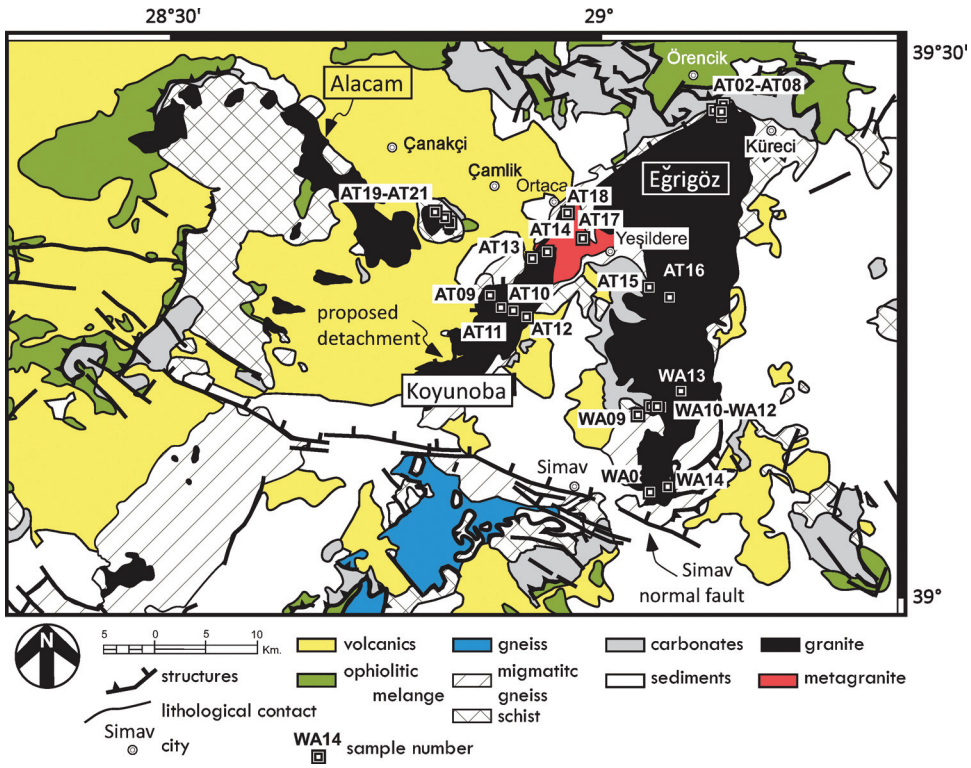

Fig. 2. Geologic map of the field area (Konak, 2002; Ring and Collins, 2005). The plutons and sample locations are indicated.

trending magmatic belt of Oligo-Miocene age (fig. 1) (for example, Delaloye and Bingöl, 2000; Özgenç and Ilbeyli, 2008). Structurally, they are bound to the north by Kütahya Fault Zone and to the south by the Simav Fault Zone, both of which have normal senses of motion (fig. 1) (Ulusay and others, 2004; Orhan and others, 2007; Özburan and Gürer, 2011).

The Eğrigöz, Koyunoba, and Alaçam plutons have been the focus of many field-based, geochemical and geochronological studies, but conflicting ideas about the nature of their compositions, ages, and relationship to a proposed detachment fault in the area exist. This paper attempts to clarify these issues using fieldwork, geochemical analyses, cathodoluminescence (CL) imaging, and *in situ* (in thin section) ion microprobe zircon geochronology. This is the first time thin section-scale CL imaging and *in situ* zircon dating has been applied to these rocks. The correlation of ages with rock- and grain-scale microstructures seen using CL is a powerful means deciphering tectonomagmatic history of the region.

GEOLOGICAL BACKGROUND

Regional Geology

Turkey is an amalgamation of multiple crustal fragments due to the closure of branches of Tethyan oceans (Okay, 2008). The İzmir-Ankara-Erzincan Suture Zone marks the closure of the Neo-Tethys and separates the Pontide region with Laurasian affinities from the Anatolide-Tauride block, which contains rocks associated with

Gondwana (fig. 1) (Ketin, 1966; Şengör and others, 1980; Okay, 1984, 1986, 2008; Moix and others, 2008). The Menderes Massif, Tavşanlı and Afyon Zones are part of the Anatolide-Tauride block, whereas the Sakarya and Rhodope Zones are part of the Pontides (fig. 1). Crust in the Menderes Massif thickened due to the closing of the Neo-Tethys during the Paleocene-Eocene along the İzmir-Ankara-Erzincan Suture Zone (Şengör and Yilmaz, 1981; Görür and others, 1984). This process is evidenced by S-vergent thrusting of large-scale nappes in the Menderes Massif (Gessner and others, 2001). Post-collisional extension exhumed the Menderes Massif and several other core complexes throughout the Aegean region, including the Rhodope, Kazdag, Cyclades, and Crete massifs (Buick, 1991; Dinter and Royden, 1993; Gautier and Brun, 1994; Jolivet and others, 1994; Kilias and others, 1994; Vandenberg and Lister, 1996; Okay and Satır, 2000). The cause of extension in the Menderes and Aegean region is generally attributed to the roll back of the African slab along the Hellenic arc, which separates the African plate from Eurasia and the Anatolian block (Seyitoğlu and Scott, 1996; Meijer and Wortel, 1997; ten Veen and Postma, 1999; Laigl and others, 2004; Cemen and others, 2006; Bonev and Beccaletto, 2007; Dilek and Sandvol, 2009).

The Eğrigöz, Koyonba, and Alaçam plutons are the largest exhumed granitoid bodies in the Menderes Massif (figs. 1 and 2) (Işık and others, 2004a, 2004b; Hasözbek and others, 2010). They intrude rocks of the Menderes Massif after the area experienced regional metamorphism (Akay, 2009). The Simav Metamorphic Sequence is the structurally lowest country rock unit exposed in the field area, and is comprised of muscovite ± biotite ± garnet schists, quartzite, and chlorite-bearing calc-schists (Kaya, 1972; Akdeniz and Konak, 1979; Özgenç and Oyman, 2004). Migmatitic-banded and biotite gneiss, marble and amphibolite are also reported from this unit (Işık and others, 2003). Conformably overlying the Simav Metamorphic Sequence is the Balıkbaşi Formation, which is laminated, bituminous, recrystallized limestone of neritic facies (Akdeniz and Konak, 1979; Oyman and others, 2012). This unit is unconformably overlain by the upper Paleozoic-lower Triassic Sarıcasu Formation, which is comprised of greenschist-grade schists with protoliths of detrital sediments, basic tuffs, and lavas (Oyman and others, 2012). The Arikaya Unit overlies the Saricasu formation and contains meta-carbonate rocks and pelitic schists that enclose limestone lenses (Akdeniz and Konak, 1979).

Geochronology and Geochemistry

Figure 1 shows the distribution of granites in western Turkey with reference to the generally accepted time frame at which they crystallized. Eocene to Oligo-Miocene subalkaline medium- to high-K and calc-alkaline granitoids in this figure are generally ascribed to have formed in a collisional regime during closure of the Neo-Tethyan ocean potentially due to increased asthenospheric heat from lithospheric Hellenic slab break-off (Genç, 1998; Dilek and Altunkaynak, 2007). Recent mantle tomography beneath western Turkey has been interpreted to show the subducted African lithosphere intruded by hot asthenosphere material (Biryol and others, 2011). Middle Miocene granitoids then formed during subsequent extension, which also produced extrusive mildly alkaline rocks with Ocean Island Basalt (OIB)-like geochemical signatures (Dilek and Altunkaynak, 2007).

Although the generation of the Northern Menderes plutons is often attributed to be the result of the second pulse of magmatism during the Middle Miocene (Akay, 2009), their reported ages are inconsistent with a single population (fig. 3). Miocene ages from the Eğrigöz, Koyunoba, and Alaçam granitoids are often attributed to their crystallization and exhumation via faulting (Işık and others, 2004a, 2004b; Ring and Collins, 2005). Some report Cretaceous (70 ± 7 Ma, Burkut, 1966 and 93 ± 1 Ma, U-Pb zircon, Ring and Collins, 2005) and Oligocene ages from these rocks (fig. 3, also review by Bozkurt and others, 2011), which are of unknown significance and some may be due

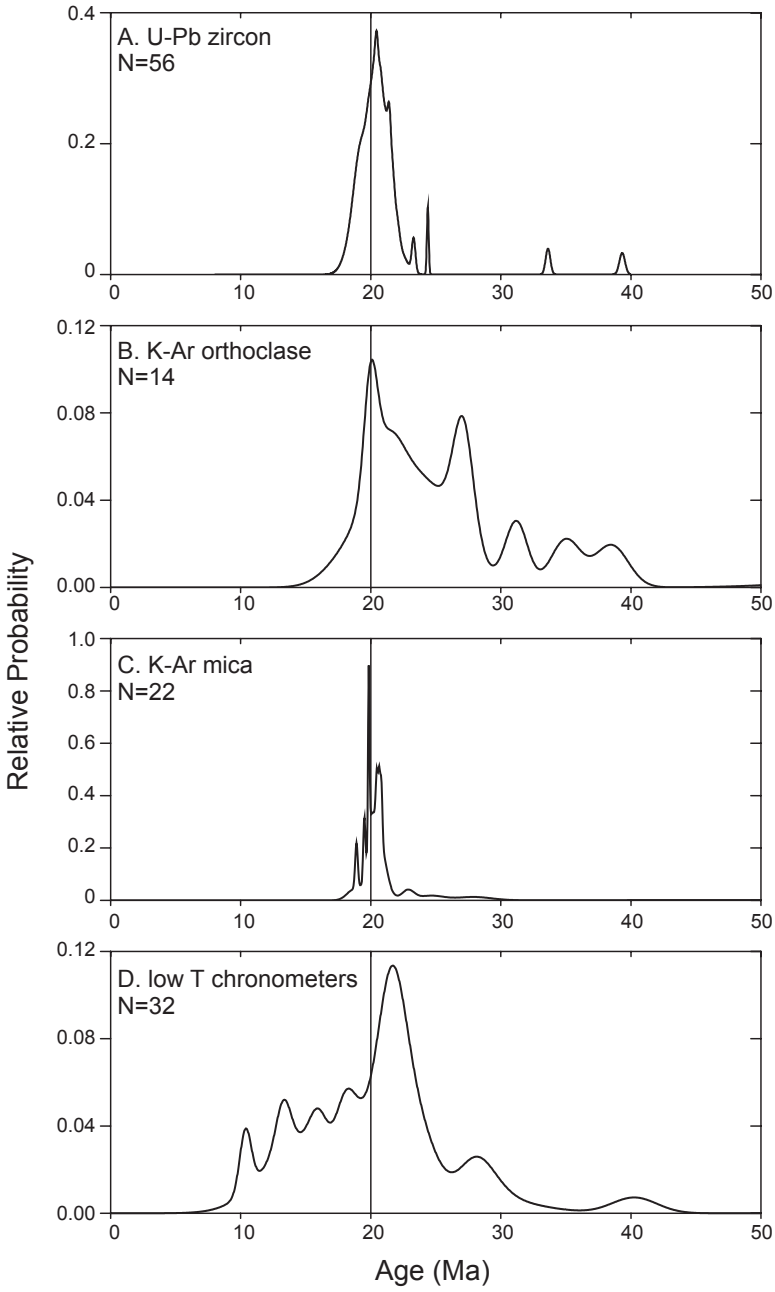

Fig. 3. Relative probability diagrams of reported ages for the Eğrigöz, Alaçam, and Koyunoba plutons using (A) ^{238}U-^{206}Pb zircon, (B) K-Ar and ^{40}Ar/^{39}Ar orthoclase and (C) K-Ar and ^{40}Ar/^{39}Ar biotite, and (D) U-Th/He apatite, and apatite and zircon fission track systems. In these diagrams, peak height is proportional to the probability the age is present in the rock and the area under the curve is equal to 1 (Ludwig, 2012; Jones and others, 2009). Data sources: Bingöl and others (1982), Delaloye and Bingöl (2000), Işık and others (2004a), Ring and Collins (2005), Thomson and Ring (2006), Erkül (2010), Hasözbek and others (2010), and Altunkaynak and others (2012). "N" means number of analyses.

to analytical problems. However, these ages are similar to those reported for granitoids elsewhere in Turkey, including the Early to Late Cretaceous Orhaneli, Topuk, and Göynükbelen plutons located ~30 to 50 km north of the field area and the Kestanbol, Eybek, and Kozak granitoids of Turkey's Biga Peninsula (fig. 1) (Delaloye and Bingöl, 2000). Thus, the Menderes plutons may contain input from sources not yet recognized.

The oldest reported ages from these rocks are Archean and Cambrian obtained via U-Pb zircon geochronology (Ring and Collins, 2005), and are likely inherited or entrained. An Archean grain from the Eğrigöz pluton has a 21.5 ± 0.7 Ma rim, likely the largest age range ever reported for a single zircon (Ring and Collins, 2005) and suggests the melts did not reach temperatures sufficient to fully dissolve xenocrystic zircon (Scott and others, 2011). In terms of their lower temperature history, U-Th/He, apatite and zircon fission track ages from the Eğrigöz and Koyunba plutons (Thomson and Ring, 2006) are, in some cases, older than their reported zircon crystallization ages (fig. 3). Bozkurt and others (2011) suggest the latest Miocene ages from these chronometers that are consistent with the results from other mineral dating systems applied to the same rocks should be considered reliable. Rb-Sr ages of 12 to 10 Ma from mylonites south of the field area are attributed to fluid-rock deformation that occurred during fault-related exhumation along the Simav detachment fault (Bozkurt and others, 2011).

In terms of composition, the granitoids have been reported to range from calc-alkaline to shoshonitic. The Eğrigöz pluton has been most analyzed and is metaluminous or peraluminous depending on sampling locality (Özgenç and Ilbeyli, 2008; Akay, 2009; Dilek and others, 2009; Ilbeyli and Kibici, 2009). Both I-type and S-type granites have been reported from the pluton (Işık and others, 2004b; Özgenç and Ilbeyli, 2008; Dilek and others, 2009; Ilbeyli and Kibici, 2009). Heterogeneities within these rocks may be caused by magma mixing, partial melting, crustal contamination, and post-emplacement fluid interactions (for example, Hibbard, 1981; Catlos and others, 2010, 2011).

The Simav Detachment Debate

These plutons are located in the hanging wall of the Simav normal fault, a high-angle (~45-60°, Seyitoğlu, 1997) north-dipping listric fault that extends ~150 km (figs. 1 and 2) (Seyitoğlu, 1997; Ersoy and others, 2010). The Simav normal fault has several kilometers of offset between the top of the hanging-wall and footwall and dips steeply to the north, roughly perpendicular to the direction of maximum extension (Seyitoğlu, 1997; Tekeli and others, 2001; Işık and others, 2003; Faulds and others, 2009). This structure formed during Pliocene to recent extension (Seyitoğlu, 1997; Ring and Collins, 2005) and is part of a region dominated by active normal faults as evidenced by a magnitude 5.8 (Mw) earthquake with a normal sense of motion that occurred near the fault on May 19, 2011 (Demirci and others, 2012).

Explanations of the plutons' exhumation mechanisms vary depending on the existence of a second extensional structure, the Simav detachment, which has been mapped trending NE-SW along the western border of the Eğrigöz and/or Koyunoba plutons (fig. 2) (Işık and Tekeli, 2001; Işık and others, 2004a; Seyitoğlu and others, 2004; Ring and Collins, 2005; Thomson and Ring, 2006). Although it has been defined as marking the lower bound of the İzmir-Ankara-Erzincan Suture Zone (Ersoy and others, 2010), the presence of this structure is debated (Özgenç and Ilbeyli, 2008; Akay, 2009). Field evidence for the detachment are high pressure/low temperature (HP/LT) metamorphic rocks thrust over the underlying rocks of the Menderes nappes (Ring and others, 2003; Akay, 2009) and metagranites interpreted as synkinematically deformed upper portions of the Eğrigöz and Koyunoba plutons (Işık and Tekeli, 2001; Işık and others, 2004a; Seyitoğlu and others, 2004; Thomson and Ring, 2006). The

detachment may have been active between 24 to 19 Ma (Ring and Collins, 2005) and accommodated ~50 km of NE-SW extension (Tekeli and others, 2001; Işık and others, 2003).

However, some regional maps show no offset between the Eğrigöz and Koyunoba and surrounding metamorphic rocks and no evidence for this structure (Işık and others, 2004b; Özgenç and Ilbeyli, 2008; Akay, 2009). Thrust faults and roof pendants from the Afyon Zone have been reported near the western boundary of the Eğrigöz and eastern boundary of the Koyunoba plutons, and between Menderes metamorphic rocks and a meta-rhyolite unit (Akay, 2009). The role of the Simav detachment as a major exhumation mechanism for these rocks is unresolved as the precise location and extent, and even the presence of this structure is unclear.

To clarify the conflicting geochemical data, unclear structural relationships, and a range of reported ages from the Eğrigöz, Koyunoba, and Alaçam plutons, we report new results from fieldwork, geochemical analyses, CL imaging, and *in situ* ion microprobe zircon geochronology.

METHODS

In the field, we focused on three specific transects: (1) from the town of Küreci to Örencik, (2) from Yeşildere to Ortaca, (3) and from Çamlık to Çanakçi (fig. 2). Five contacts of the plutons were crossed, two of which were exposed. Overall, 30 samples from 26 locations were obtained (fig. 2; table 1). Thin sections were examined using an optical microscope to determine mineral assemblages (table 1).

Major and trace element geochemical analyses of the Eğrigöz, Koyunoba, and Alaçam plutons were performed at Activation Laboratories in Ontario, Canada (tables 2, 3, 4, 5 and 6; figs. 4, 5 and 6). Abundances of Sc, Be, V, Ba, Sr, Y, and Zr were measured using whole rock fusion inductively coupled plasma (ICP) methods; all other elements were obtained using whole rock fusion ICP mass spectrometry. We also estimated zircon saturation temperatures for each rock using the major and trace element data (tables 2-6) (Watson and Harrison, 1983).

Entire rock thin sections were imaged using CL with a Premier American Technologies Luminoscope model ELM-3R in the Smithsonian Institution's Department of Mineral Sciences at the National Museum of Natural History using the methods as outlined by Sorensen and others (2006) (figs. 7, 8, 9, 10, 11, 12, and 13). An electron beam was run with operating conditions of 20 kV and 0.5 mA. Using a rotating red-blue-green (R-G-B) color filter wheel, three images are captured with a 1300 × 1030 pixel monochrome charged-coupled device. MagnaFire software combines the three R-G-B images to produce the final image. Exposure time varied between 30 seconds to 3 minutes depending on the sample.

CL is used to understand the history of the Eğrigöz, Koyunoba, and Alaçam plutons by identifying mineral distribution and compositions, rock textures, mineral zoning, and evidence fluid alteration (Ramseyer and others, 1992; Cox and others, 1996; Stirling and others, 1999; Goetze and others, 2000; Sorensen and others, 2006). Minerals imaged in the Eğrigöz, Koyunoba, and Alaçam plutons show characteristic colors. Plagioclase grains are shades of green due to the presence of Ca^{2+} and Mn^{2+} (for example, Geake and others, 1973; Catlos and others, 2011). Alkali feldspars are blue due to activators Eu^{2+}, Ti^{4+}, and Ga^{3+} (Geake and others, 1973; Mariano and Ring, 1975; De St. Jorre and Smith, 1988; Finch and Klein, 1999; Parsons and others, 2008). K-feldspar can turn red (from blue) due to trace amounts of Fe changing oxidation state (Finch and Klein, 1999). In igneous rocks, quartz only weakly luminesces and is seen as brown or dull black. Subtle variations of colors in feldspars and quartz are typically attributed to different amounts of activators and quenchers and may distinguish different generations of crystallization (Marshall, 1988). Bright yellow apatite and bright white zircon grains are also visible in the thin-section scale CL

TABLE 1

Sample locations and mineral assemblages of rocks collected in this study

Sample	Location	Mineral assemblage[a]
		Eğrigöz
AT02B	39°26'02.60"N, 29°07'00.50"E	Qtz+Pl+Kfs+Bt+Ms+Hbl+Chl+Aln+Ap +Zrn+Mnz+Hem+Cal
AT03	39°25'37.90"N, 29°07'22.40"E	Qtz+Pl+Kfs+Bt+Ms+Hbl+Chl+Ep+Cal+Zrn
AT04A	39°25'42.10"N, 29°07'18.20"E	Qtz+Pl+Kfs+Bt+Chl+Hbl+Ap+Cal +Zrn
AT04B	same as AT04A	Qtz+Pl+Kfs+Bt+Ms+Chl+Hbl+Hem+Zrn
AT05A[b]	39°25'43.40"N, 29°07'18.20"E	Qtz+Pl+Kfs+Bt+Ab+Hbl+Chl+Ap+Zrn+Rt+Cal+Hem+Aln
AT05B	same as AT05A	Qtz+Pl+Kfs+Bt+Chl+Hbl+Zrn+Hem
AT06	39°25'49.30"N, 29°07'15.50"E	Qtz+Pl+Kfs+Bt+Chl+Hem+Ap+Zrn+Ttn
AT07A	39°26'08.60"N, 29°07'21.80"E	Qtz+Pl+Kfs+Bt+Ms+Hem+Zrn
AT08	39°26'02.60"N, 29°07'00.50"E	Qtz+Pl+Kfs+Bt+Chl+Zrn
AT15A	39°16'22.00"N, 29°01'36.40"E	Qtz+Pl+Kfs+Bt+Ms+Zrn
AT15B	same as AT15A	Qtz+Pl+Kfs+Bt+Ms+Chl+Hem+Zrn
AT15C	same as AT15A	Qtz+Pl+Kfs+Bt+Ms+Chl+Hem+Zrn
AT16[b]	39°16'30.10"N, 29°03'25.50"E	Qtz+Pl+Kfs+Bt+Ap+Chl+Ms+Zrn
WA08	39° 04'14.20"N, 29°03'22.60"E	Qtz+Pl+Kfs+Bt+Ms+Ab +Ap+Zrn+Ilm+Ttn+Hem+Brt+Rt
WA09B	39°08'08.60"N, 29°02'00.20"E	Qtz+Pl+Kfs+Bt+Ms+Chl+Sil+Zrn+Mnz+Ilm+Rt
WA10B	39°08'35.10"N, 29°02'42.90"E	Qtz+Pl+Kfs+Bt+Aln+Zrn+Ap+Th+Rt+Ttn+Hem
WA12B[b]	39°08'34.90"N, 29°03'24.70"E	Qtz+Pl+Kfs+Bt+Ms+Ab+Ap+Hem+Zrn
WA13B	39°09'32.20"N, 29°04'46.40"E	Qtz+Pl+Kfs+Bt+Opx+Cpx+Ab +Ms+Ilm+Ap+Aln+Brt+FeO+Rt+Th
WA14	39°04'38.00"N, 29°05'16.70"E	Qtz+Pl+Kfs+Bt+Ms+Chl+Hbl +Ap+Zrn+Ilm+Brt+FeO
		Koyunoba
AT09	39°14'21.50"N, 28°51'36.50"E	Qtz+Pl+Kfs+Bt+Ms
AT10	39°13'48.50"N, 28°52'20.30"E	Qtz+Pl+Kfs+Bt+Ms+Ap+Zrn+Mnz+Hem
AT11	39°13'23.20"N, 28°53'00.40"E	Qtz+Pl+Kfs+Bt+Cal+Hem
AT12[b]	39°13'07.10"N, 28°53'43.60"E	Qtz+Pl+Kfs+Bt+Zrn+Ap+Hem+Chl+Ms+Hbl
AT13	39°17'08.70"N, 28°54'39.40"E	Qtz+Pl+Kfs+Bt+Ms+Chl+Ap+Hem+Zrn
AT14[b]	39°16'59.06"N,28°54'30.70"E	Qtz+Pl+Kfs+Bt+Ab+Ms+Hem+Ap+Ilm+Rt+Zrn+Mnz
AT17	39°18'35.40"N, 28°57'35.10"E	Qtz+Pl+Kfs+Bt+Chl+Hem+Zrn
		Alaçam
AT19[b]	39°20'22.30"N, 28°49'01.20"E	Qtz+Pl+Kfs+Bt+Ap+Zrn+Rt+Cal+Hem+Hbl+Ms
AT20A[b]	39°20'34.60"N, 28°68'31.80"E	Qtz+Pl+Kfs+Bt+Ilm+Ms+Rt+Ap+Cal+Zrn+Hem+Chl+Aln
AT20B[b,c]	same as AT20A	Qtz+Pl+Kfs+Bt+Ms+Rt+Cal+Zrn+Hem
AT21	39°20'49.00"N, 28°47'59.50"E	Qtz+Pl+Ksp+Bt+Chl+Hbl+Zr+Hem

[a] Abbreviations after Siivola and Schmid (2007).
[b] Zircon dated in this rock.
[c] Volcanic, extrusive sample.

images. Calcite, a secondary mineral acquired during fluid alteration, is bright orange and is typically located along microcracks and grain boundaries. Biotite, muscovite, hornblende, rutile, and monazite are not visible in CL.

Eight samples were collected for *in situ* U-Pb zircon geochronology (fig. 2; tables 7, 8, 9, 10 and 11). Samples AT05A, AT16, and WA12B are from the northern, central, and southern sections of the Eğrigöz pluton. Sample AT12 is located on the eastern

TABLE 2

Major and trace element concentrations from samples of the Northern Eğrigöz pluton[a]

Analyte Symbol	AT02B	AT03	AT04A	AT04B	AT05A	AT05B	AT06	AT07A	AT08
SiO_2	71.12	67.90	68.63	66.39	68.56	68.88	70.96	69.81	71.37
Al_2O_3	14.76	15.48	14.67	15.23	14.85	14.82	14.94	14.83	14.71
Fe_2O_3(T)	2.17	1.82	3.48	3.89	3.05	3.02	2.87	2.64	2.62
MnO	0.047	0.027	0.036	0.026	0.026	0.023	0.042	0.030	0.030
MgO	0.68	1.01	0.89	1.16	1.03	0.94	0.67	0.66	0.66
CaO	1.06	3.19	2.44	2.56	2.94	2.54	2.05	2.15	1.89
Na_2O	3.72	4.53	3.44	3.40	3.78	3.34	3.75	3.71	3.82
K_2O	4.25	3.45	4.41	4.57	3.37	4.60	4.09	4.33	3.84
TiO_2	0.345	0.445	0.390	0.509	0.445	0.416	0.329	0.343	0.319
P_2O_5	0.14	0.14	0.12	0.17	0.15	0.15	0.12	0.14	0.13
LOI[b]	1.90	1.12	1.00	0.80	0.92	0.93	0.72	1.07	0.94
Total	100.2	99.1	99.5	98.7	99.1	99.7	100.5	99.7	100.3
Sc	6	8	5	7	7	7	6	6	5
Be	4	3	3	3	3	3	4	4	6
V	27	51	39	53	44	43	23	25	24
Ba	794	1249	1566	1318	658	1195	758	948	733
Sr	176	304	269	271	276	264	210	229	210
Y	26	22	23	21	22	18	25	27	26
Zr	165	169	170	193	172	141	157	163	160
Co	2	1	3	3	3	2	2	2	2
Cu	< 10	< 10	< 10	< 10	< 10	< 10	< 10	< 10	10
Zn	< 30	< 30	< 30	< 30	< 30	< 30	< 30	30	30
Ga	17	17	16	17	17	16	17	17	17
Ge	2	2	2	2	2	2	2	2	2
Rb	142	88	152	150	128	138	163	156	137
Nb	14	13	14	14	13	12	14	14	16
Mo	< 2	< 2	< 2	< 2	< 2	4	3	< 2	< 2
Ag	0.5	0.6	0.5	0.6	0.6	< 0.5	0.5	0.5	< 0.5
Sn	6	9	4	5	5	6	5	6	5
Cs	2.1	1.5	4.9	4.8	4.8	3.7	10.3	5.3	4.7
La	72.1	63.6	34.3	53	33.9	33.4	38.8	38.1	30.3
Ce	136	115	66.2	100	65.2	63.2	75.5	73.1	56.9
Pr	13.4	11.3	6.94	10	6.84	6.57	7.84	7.59	6.18
Nd	44.7	38	24.4	34.6	24.4	22.7	27.7	26.6	22.5
Sm	7.6	6.2	4.7	6	4.6	4.4	5.4	5.2	4.8
Eu	0.87	1.14	1	1.12	0.99	1.04	0.85	0.9	0.86
Gd	5.6	4.6	4	4.9	4	3.7	4.4	4.5	4.3
Tb	0.9	0.7	0.7	0.7	0.6	0.6	0.7	0.8	0.7
Dy	4.9	4	3.9	3.9	3.7	3.5	4.3	4.7	4.3
Ho	1	0.8	0.8	0.8	0.8	0.7	0.9	1	0.9
Er	2.9	2.4	2.4	2.2	2.3	2.1	2.6	3	2.6
Tm	0.44	0.36	0.38	0.33	0.35	0.31	0.4	0.46	0.4
Yb	2.9	2.4	2.7	2.2	2.3	2.1	2.7	3.1	2.8
Lu	0.48	0.39	0.46	0.35	0.37	0.34	0.45	0.5	0.46
Hf	4.7	4.8	4.9	5.4	5	4.1	4.5	4.9	4.8
Ta	1.5	1	1.5	0.9	1.1	1	1.6	1.5	2.2
Tl	0.8	0.4	0.7	0.8	0.6	0.7	0.8	0.8	0.7
Pb	23	22	42	28	22	28	31	35	31
Th	26.7	29.6	18.9	22.1	19.5	18.1	23.3	20.1	25.5
U	6.4	6.2	7.4	4.4	6.7	5.1	8	10.1	8.3
Sat T(°C)[c]	798	768	780	789	780	764	781	780	785

[a] Elements measured but not detected include Cr, Ni (<20 ppm detection limits), As (<5 ppm), In (<0.2 ppm), Sb (<0.5 ppm), W (<1 ppm), and Bi (<0.4 ppm).
[b] LOI = loss on ignition.
[c] Zircon saturation temperature (Watson and Harrison, 1983).

TABLE 3

Major and trace element concentrations from samples of the central section of the Eğrigöz pluton[a]

Analyte Symbol	AT15A	AT15B	AT15C	AT16
SiO_2	72.39	71.34	70.87	70.83
Al_2O_3	14.37	14.42	14.75	14.06
Fe_2O_3(T)	2.79	3.09	2.75	3.48
MnO	0.047	0.051	0.045	0.050
MgO	0.69	0.78	0.73	0.81
CaO	1.77	1.93	2.02	1.95
Na_2O	3.53	3.52	3.7	3.03
K_2O	4.15	4.21	3.90	4.87
TiO_2	0.332	0.371	0.350	0.377
P_2O_5	0.15	0.15	0.13	0.11
LOI[b]	0.71	0.82	0.78	0.74
Total	100.9	100.7	100.0	100.3
Sc	6	6	5	6
Be	3	4	3	3
V	25	26	25	40
Ba	971	935	899	781
Sr	210	219	236	210
Y	22	22	18	16
Zr	159	167	166	148
Co	2	3	2	3
Cu	< 10	< 10	10	< 10
Zn	40	50	60	50
Ga	17	16	17	15
Ge	2	2	2	2
Rb	170	159	143	169
Nb	13	15	11	12
Mo	3	< 2	< 2	< 2
Ag	0.5	< 0.5	0.5	< 0.5
Sn	5	5	5	3
Cs	6.5	11.5	7.9	5.9
La	33.9	34.6	36.4	44.6
Ce	64.7	66.6	69.1	81
Pr	6.77	7.06	7.14	7.86
Nd	24	24.9	24.8	26
Sm	4.8	4.9	4.7	4.3
Eu	0.9	0.9	0.95	0.86
Gd	4.1	4.2	4	3.2
Tb	0.7	0.7	0.6	0.5
Dy	3.8	4	3.6	3
Ho	0.8	0.8	0.7	0.6
Er	2.2	2.3	2.1	1.8
Tm	0.34	0.36	0.31	0.28
Yb	2.3	2.4	2.1	1.9
Lu	0.39	0.4	0.34	0.33
Hf	4.5	4.7	4.6	4.2
Ta	1.2	1.3	1.1	1.2
W	2	1	< 1	< 1
Tl	0.8	0.8	0.7	0.8
Pb	34	29	41	34
Th	18.8	18.5	18.2	84.3
U	7.6	6.3	6.2	13.8
Sat T(°C)[c]	786	787	788	774

[a] Elements measured but not detected include Cr, Ni (<20 ppm detection limits), As (<5 ppm), In (<0.2 ppm), Sb (<0.5 ppm), and Bi (<0.4 ppm).
[b] LOI = loss on ignition.
[c] Zircon saturation temperature (Watson and Harrison, 1983).

Table 4

Major and trace element concentrations from samples of the southeastern portion of the Eğrigöz pluton[a]

Analyte Symbol	WA08	WA09B	WA10B	WA12B	WA13B	WA14
SiO_2	64.75	70.05	76.69	70.52	71.90	72.11
Al_2O_3	15.27	14.25	11.66	14.48	13.39	13.45
Fe_2O_3(T)	6.57	3.24	1.32	2.83	2.33	2.42
MnO	0.061	0.047	0.017	0.050	0.038	0.038
MgO	2.29	1.25	0.12	0.67	0.48	0.68
CaO	2.46	1.89	0.38	2.10	1.39	1.77
Na_2O	3.11	3.77	2.78	3.29	2.93	3.09
K_2O	2.47	2.44	5.54	4.45	4.82	4.55
TiO_2	0.819	0.427	0.078	0.331	0.264	0.379
P_2O_5	0.34	0.05	0.03	0.11	0.08	0.12
LOI[b]	2.32	1.12	0.52	0.94	0.8	0.96
Total	100.5	98.5	99.1	99.8	98.4	99.6
Sc	16	7	1	7	5	7
Be	2	3	2	3	3	3
V	125	57	< 5	40	25	36
Ba	581	499	140	929	608	1123
Sr	302	257	81	213	129	194
Y	34	11	18	25	17	23
Zr	175	143	140	171	127	180
Cr	80	40	< 20	< 20	< 20	< 20
Co	16	9	1	3	2	3
Ni	30	< 20	< 20	< 20	< 20	< 20
Cu	70	10	< 10	< 10	< 10	< 10
Zn	60	180	< 30	30	< 30	< 30
Ga	17	16	16	15	15	15
Ge	2	2	2	2	2	2
As	8	< 5	< 5	10	< 5	< 5
Rb	86	90	134	167	172	141
Nb	10	14	11	14	13	14
Ag	0.9	0.9	0.7	0.9	0.6	0.8
Sn	4	3	2	3	3	5
Cs	6	2.8	0.7	5.7	6.3	3.5
La	36.8	26.7	37.6	39.7	39.9	53.9
Ce	74.6	48.8	54.5	72.2	75.7	103
Pr	8.71	5.08	8.26	7.98	8.05	10
Nd	30.5	16.2	26.6	25.3	24.3	30.1
Sm	6.5	3	6.2	5	4.6	5.4
Eu	1.75	1.18	0.23	0.91	0.64	0.92
Gd	6.3	2.7	5.5	4.5	3.6	4.5
Tb	1	0.4	0.8	0.7	0.5	0.7
Dy	6.2	2.2	4.2	4.4	3.1	4.1
Ho	1.2	0.4	0.7	0.9	0.6	0.8
Er	3.5	1.2	1.8	2.7	1.9	2.4
Tm	0.53	0.19	0.26	0.42	0.3	0.37
Yb	3.6	1.3	1.6	3.1	2.1	2.6
Lu	0.57	0.21	0.24	0.55	0.35	0.43
Hf	4.6	4.2	6.3	5.2	4.1	4.8
Ta	0.7	1.3	1	2.1	1.3	1.2
W	< 1	< 1	< 1	2	< 1	< 1
Tl	0.6	0.5	0.4	0.7	0.7	0.6
Pb	21	88	15	34	34	28
Th	6.8	9	23.2	19	29.8	29.3
U	2.5	2.8	1.8	3.8	5.4	6.2
Sat T(°C)[c]	802	785	780	788	769	794

[a] Elements measured but not detected include Mo (<2 ppm detection limits), In (<0.2 ppm), Sb (<0.5 ppm), and Bi (<0.4 ppm).
[b] LOI = loss on ignition.
[c] Zircon saturation temperature (Watson and Harrison, 1983).

TABLE 5

Major and trace element concentrations from samples of the Koyunoba pluton[a]

Analyte Symbol	AT09	AT10	AT11	AT12	AT13	AT14	AT17
SiO_2	74.52	72.75	73.76	65.47	70.98	70.5	72.14
Al_2O_3	13.55	13.79	13.52	16.60	15.10	15.09	14.04
Fe_2O_3(T)	2.21	2.67	2.34	4.84	2.73	3.38	1.71
MnO	0.07	0.047	0.050	0.057	0.054	0.054	0.023
MgO	0.20	0.34	0.16	1.57	0.71	0.69	0.42
CaO	0.90	1.06	0.68	3.82	1.97	2.08	1.46
Na_2O	3.95	3.91	3.46	3.55	3.71	3.99	3.45
K_2O	4.57	4.56	4.92	3.28	4.23	3.97	4.77
TiO_2	0.121	0.174	0.102	0.481	0.332	0.351	0.211
P_2O_5	0.04	0.09	0.05	0.24	0.16	0.16	0.13
LOI[b]	0.51	0.71	0.99	0.77	0.58	0.68	0.54
Total	100.6	100.1	100.0	100.7	100.6	100.9	98.9
Sc	4	4	4	8	5	5	4
Be	5	5	4	4	3	4	3
V	< 5	9	< 5	65	23	22	15
Ba	748	796	788	1637	974	1130	795
Sr	99	118	66	758	279	294	205
Y	29	25	23	23	20	21	18
Zr	134	142	129	144	171	211	106
Co	< 1	1	< 1	5	3	2	1
Cu	10	< 10	10	10	< 10	< 10	< 10
Zn	40	40	50	50	< 30	50	< 30
Ga	17	17	16	18	17	17	15
Ge	2	2	2	2	2	2	2
Rb	177	179	185	105	154	135	137
Nb	17	20	16	14	14	16	14
Mo	< 2	< 2	< 2	< 2	< 2	< 2	3
Ag	< 0.5	< 0.5	< 0.5	< 0.5	0.5	0.6	< 0.5
Sn	5	4	6	7	4	4	3
Cs	9	6.5	5.5	7.3	4.7	5.9	3.5
La	49.9	45.2	47.5	27.8	39.2	42.4	26
Ce	92.3	85.4	89.1	53.4	74.1	79.4	50.7
Pr	9.45	8.85	9.07	5.93	7.71	8.01	5.24
Nd	32.4	30.4	31.2	22.5	27	28.2	18.3
Sm	6	6.1	5.5	4.9	5.1	5	3.8
Eu	0.74	0.7	0.62	1.22	0.96	1	0.67
Gd	5	4.9	4.4	4.2	4.2	4.1	3.2
Tb	0.8	0.8	0.7	0.7	0.7	0.6	0.5
Dy	5.1	4.7	4.1	4	3.8	3.7	3.1
Ho	1	0.9	0.8	0.8	0.8	0.8	0.6
Er	3	2.7	2.4	2.4	2.2	2.3	1.8
Tm	0.47	0.41	0.38	0.37	0.33	0.35	0.28
Yb	3.1	2.8	2.6	2.5	2.1	2.4	1.9
Lu	0.51	0.47	0.43	0.41	0.34	0.39	0.33
Hf	4.2	4.5	4.2	4.1	4.8	5.6	3.3
Ta	2	1.9	1.5	1.4	1.3	1.3	1.7
W	2	< 1	2	< 1	< 1	< 1	< 1
Tl	0.9	0.7	0.9	0.6	0.8	0.7	0.6
Pb	40	41	50	34	43	47	54
Th	24.3	25.4	22.7	11.9	20.1	21.2	16.2
U	7.3	4.9	3.6	6.1	5	2.5	7
Sat T(°C)[c]	772	775	775	762	790	805	751

[a] Elements measured but not detected include Cr, Ni (<20 ppm detection limits), As (<5 ppm), In (<0.2 ppm), Sb (<0.5 ppm), and Bi (<0.4 ppm).

[b] LOI = loss on ignition.

[c] Zircon saturation temperature (Watson and Harrison, 1983).

TABLE 6

Major and trace element concentrations from samples of the Alaçam pluton[a]

Analyte Symbol	AT19	AT20A	AT20B[b]	AT21
SiO_2	68.07	67.59	73.94	67.5
Al_2O_3	15.42	15.37	12.65	14.68
Fe_2O_3(T)	3.61	4.22	2.47	4.46
MnO	0.068	0.076	0.068	0.066
MgO	1.00	1.21	0.49	1.29
CaO	2.78	3.07	0.25	3.02
Na_2O	3.53	3.56	0.36	3.54
K_2O	3.75	3.69	5.64	3.69
TiO_2	0.448	0.515	0.324	0.54
P_2O_5	0.14	0.18	0.09	0.17
LOI[c]	0.67	0.69	2.86	0.55
Total	99.5	100.2	99.2	99.5
Sc	7	9	5	9
Be	3	3	2	3
V	55	55	25	66
Ba	943	837	1095	919
Sr	320	320	61	303
Y	20	17	19	26
Zr	159	186	177	198
Co	4	5	2	6
Zn	60	90	80	50
Ga	17	17	14	18
Ge	2	2	2	2
As	< 5	< 5	15	< 5
Rb	127	109	231	128
Nb	13	13	16	15
Mo	< 2	< 2	9	< 2
Ag	< 0.5	0.5	0.6	0.6
Sn	4	2	3	4
Sb	< 0.5	< 0.5	5.5	< 0.5
Cs	8	5.3	20	10.2
La	21	38.3	61	108
Ce	38.6	73.3	107	194
Pr	4.93	7.62	10.4	18.6
Nd	18.9	26.6	34	59.5
Sm	4.5	5	5.7	8.7
Eu	1.13	1.1	0.82	1.19
Gd	4	4.1	4.2	6.2
Tb	0.7	0.6	0.6	0.9
Dy	4.1	3.2	3.5	4.9
Ho	0.8	0.6	0.7	1
Er	2.4	1.8	2.1	2.9
Tm	0.37	0.26	0.33	0.43
Yb	2.6	1.6	2.3	2.9
Lu	0.42	0.25	0.4	0.46
Hf	4.6	5.1	5.1	5.6
Ta	1.2	0.7	1.4	1.4
W	1	< 1	3	< 1
Tl	0.8	0.7	2.2	0.7
Pb	28	26	23	24
Th	13.4	22.8	34.3	39.7
U	6.1	4.1	9.8	6
Sat T(°C)[d]	778	786	845	787

[a] Elements measured but not detected include Cr, Ni (<20 ppm detection limits), Cu (<10 ppm), In (<0.2 ppm), and Bi (<0.4 ppm).
[b] AT20B is a volcanic sample.
[c] LOI = loss on ignition.
[d] Zircon saturation temperature (Watson and Harrison, 1983).

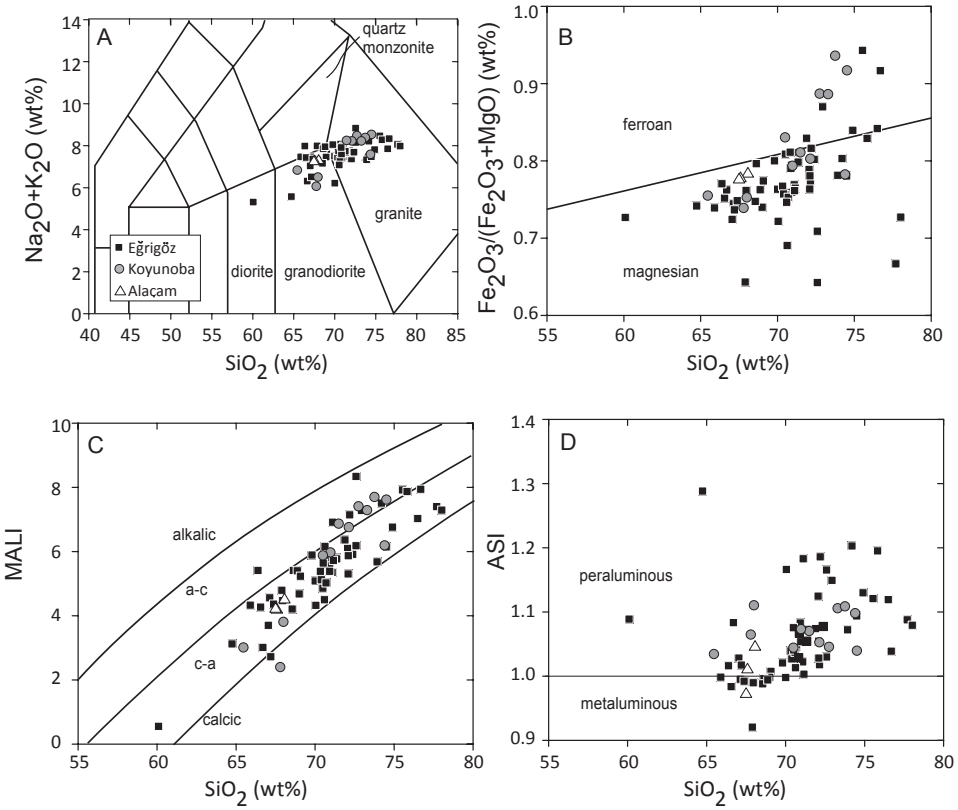

Fig. 4. (A) $Na_2O + K_2O$ (wt%) vs. SiO_2 (wt%) showing the classification fields of the Eğrigöz, Koyunoba, and Alaçam granitoids. (B) $Fe_2O_3/(Fe_2O_3 + MgO)$ vs. SiO_2 (wt%), (C) modified Alkaline Lime Index ($Na_2O + K_2O - CaO$) vs. SiO_2 (wt%), and (D) aluminosaturation index [ASI, $Al/(Ca - 1.67P + Na + K)$] vs. SiO_2 (wt%) diagram after Frost and others (2001) and Frost and Frost (2008). Abbreviations: "a-c" = alkali-calcic, "c-a" = calc-alkalic. Data includes ours, Özgenç and Ilbeyli (2008), Akay (2009), Erkül (2010), and Oyman and others (2012).

edge of the Koyunoba pluton and sample AT14 is from its northern portion. Alaçam rocks AT19, AT20A and AT20B were also selected for dating. Sample AT20B is from a rhyolite dike within the Alaçam pluton adjacent to sample AT20A. Zircons were located petrographically and using a JEOL JSM-6490 scanning electron microscope (SEM) at the Department of Geological Sciences, University of Texas at Austin. Identified grains were relocated using an optical microscope and thin sections containing the minerals were cut into small pieces. The chips were cleaned and mounted with a pre-polished block of zircon age standards (AS3, 1099 ± 1 Ma; Schneider and others, 1999).

In situ zircon ages were obtained using the high-sensitivity/high-resolution CAMECA ims1270 ion microprobe at UCLA. In this method, a 30 μm–diameter beam of oxygen primary ions bombards a sample and erodes as little as ~10Å of the sample surface during a typical 15 minute analysis. The ion microprobe operated with a running mass resolution of 4800, a primary accelerating voltage of −12.5 kV, a secondary voltage of ~10 kV, and arc current ~74.7 to 74.9 mA. To calculate the age, we use the standard age equation of:

$$t = 1/\lambda * \ln\left[1 + \left(^{206}Pb/^{238}U\right)_{cal}\right] \quad (1)$$

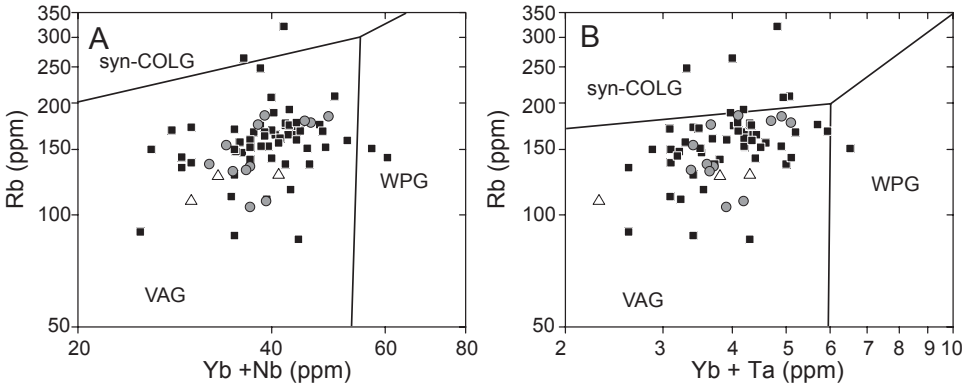

Fig. 5. Rb (ppm) vs. (A) Y + Nb (ppm) and (B) Y + Ta discrimination diagrams (Pearce and others, 1984). Data sources and symbols are the same as in figure 4. Abbreviations: "VAG" = volcanic arc, "syn-COLG" = syn-collisional, "WPG" = within plate.

where t = age (Ma), λ is the decay constant for ^{238}U (assumed to be 1.55125×10^{-4}/Ma; Steiger and Jäger, 1977) and $(^{206}Pb/^{238}U)_{cal}$ is corrected for instrument dead time, drift, common Pb and is estimated relative to the AS3 age standards. The method is similar to that described by Compston and others (1984). We used the ZIPS v.3.0.4 software written by C. D. Coath, which calculates the isotopic ratios and ages from measured ion intensities. The ion microprobe zircon calibration curve used here has an equation of:

$$UO^+/U^+ = 0.430\ (^{206}Pb^+/U^+ \text{ Relative Sensitivity Factor}) + 5.797 \pm 0.115 \qquad (2)$$

for the AS3 standard. We obtained 42 spots on the standard grains to develop the calibration curve, which reproduced the age to 1096 ± 64 Ma (±1σ).

For calculating Th/U ratios of the grains, we analyzed standard 91500 (Wiedenbeck and others, 1995) and used equation (3):

$$(Th/U)_{zircon} = [(Th/U)_{91500}/(Th^+/U^+)_{91500m}]*(Th^+/U^+)_{zircon} \qquad (3)$$

where $(Th/U)_{91500}$ is 0.35 (Wiedenbeck and others, 1995), $(Th^+/U^+)_{91500m}$ is measured in the standard grain (3.153 ± 0.006 in this study), and $(Th^+/U^+)_{zircon}$ is the measured ratio for each dated grain. In general, Th/U ratios of igneous zircons are higher than of those affected by metamorphism (Williams and Claesson, 1987; Cavosie and others, 2004).

All ages reported here are at the ±1σ level. Two major sources that may contribute to age uncertainty are: (1) if the grains contain lower amounts of radiogenic Pb (reported as $\%^{206}Pb^*$ in tables 7-9) or (2) if the dated grain's UO^+/U^+ ratio lies outside the range of the calibration curve, which ranges from 7.028 ± 0.014 to 8.634 ± 0.045 for this study. To minimize contributions of Pb outside of the dated grain, we generated an UO^+ ion image of each grain and inserted aperture windows to restrict data collection from its center portion. We use the same aperture settings for both standard and unknown analyses. These windows are essential for *in situ* analyses, as significant Pb contamination could arise if sputtered material from outside of the grain boundaries is measured.

We report two sets of $^{238}U/^{206}Pb$ ages in tables 7, 8 and 9 that have been generated using different common Pb corrections (measured ^{204}Pb, and $^{206}Pb/^{204}Pb$ methods; Faure, 1986). A similar approach is employed by Altunkaynak and others (2012). We

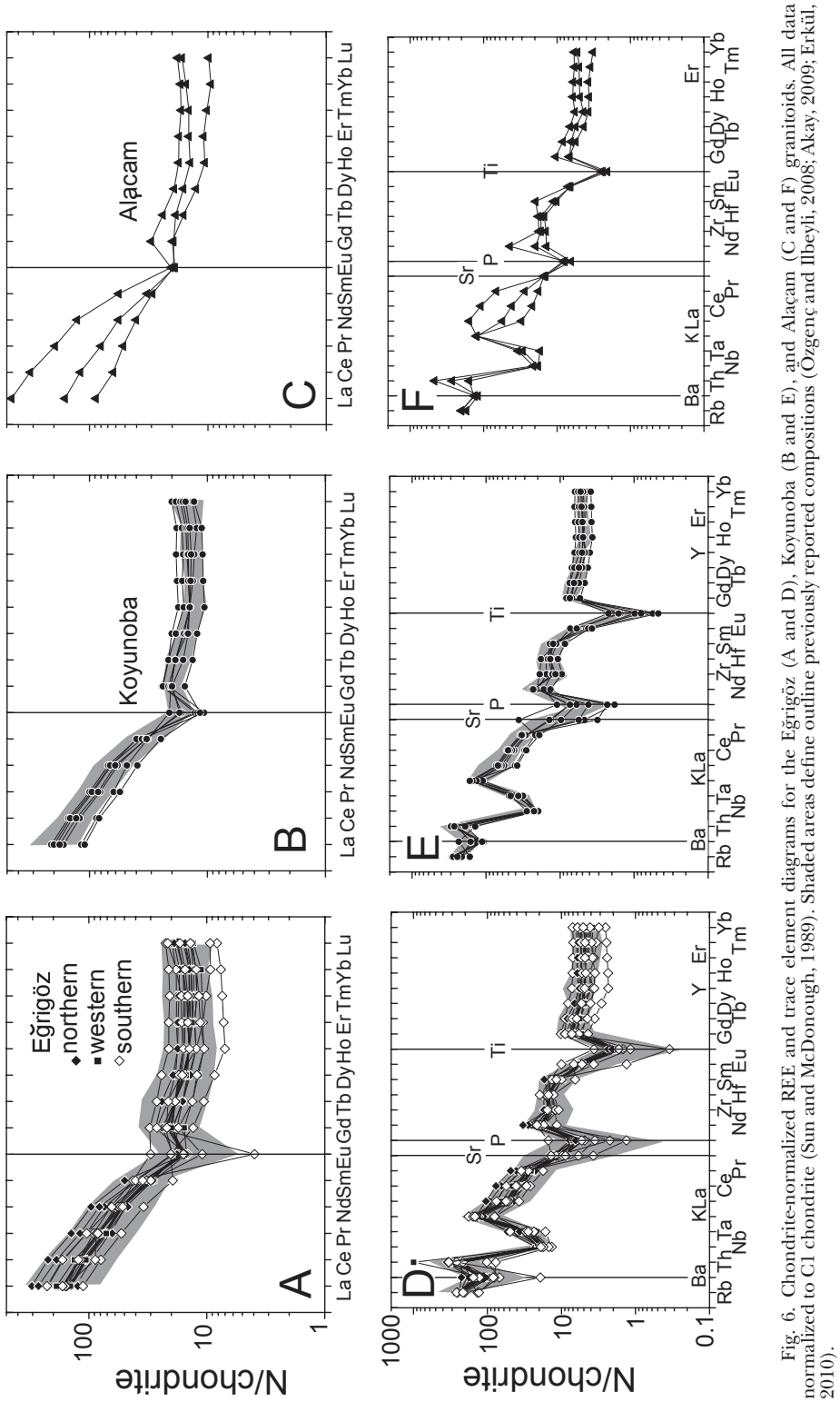

Fig. 6. Chondrite-normalized REE and trace element diagrams for the Eğrigöz (A and D), Koyunoba (B and E), and Alaçam (C and F) granitoids. All data normalized to C1 chondrite (Sun and McDonough, 1989). Shaded areas define outline previously reported compositions (Özgenç and İlbeyli, 2008; Akay, 2009; Erkül, 2010).

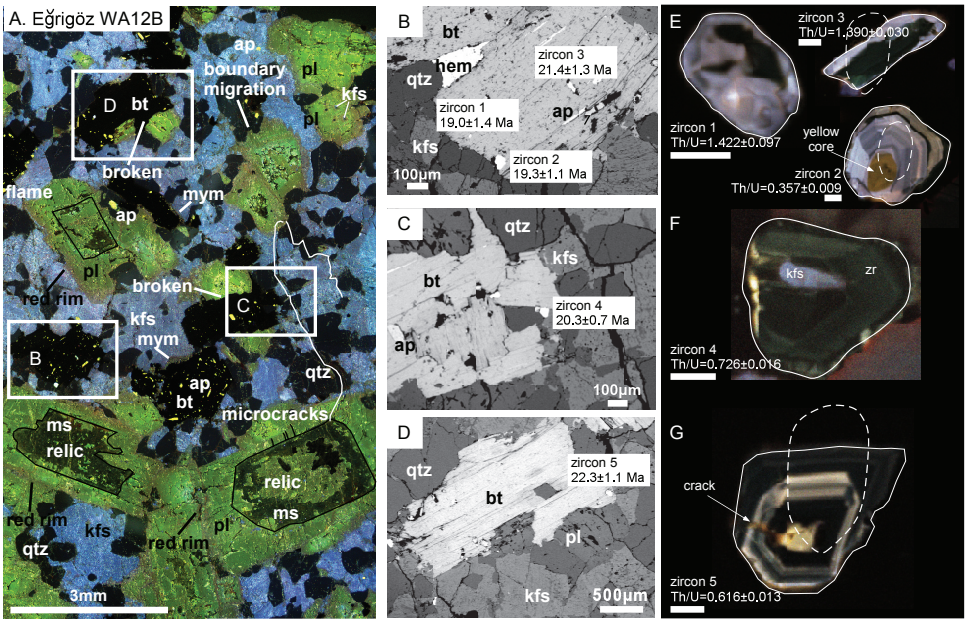

Fig. 7. (A) CL image of Eğrigöz sample WA12B. Mineral abbreviations after Siivola and Schmid (2007). Boxes indicate the locations of the backscattered electron (BSE) images in (B), (C) and (D). Abbreviations: "mym" = myrmekite. Ion microprobe $^{238}U/^{206}Pb$ ages ($\pm 1\sigma$) of the dated zircons are indicated. (E) CL images of dated zircons in panel (B). (F) CL image of dated zircon in panel (C). (G) CL image of dated zircon in panel (D). Scale bar for all zircon CL images is 10 µm. If possible, we indicate the location of the ion microprobe spot as a dashed oval.

discuss and report the $^{238}U/^{206}Pb$ ages that have been calculated using the ^{204}Pb correction in figures 7 through 14, which provides the most concordant results. In some cases, the $^{235}U/^{207}Pb$ and $^{206}Pb/^{207}Pb$ ages of the grains have high uncertainty, likely due to the small amounts of $^{207}Pb^{+}$ sputtered from the grains compared to the $^{206}Pb^{+}$ contents in the Miocene- to Oligocene-age grains. We report $^{235}U/^{207}Pb$ ages from grains with reasonable uncertainty in table 10 and a summary of all of the $^{238}U/^{206}Pb$ results corrected using the ^{204}Pb method, including average and weighted mean ages in table 11.

To assist with the interpretation of each age, dated zircons were imaged using secondary electrons and with CL using FEI Nova NanoSEM 430 with attached Gatan Chroma CL-SP detector at UT Austin's Bureau of Economic Geology (figs. 7-13). The SEM-CL operated in high vacuum mode with an accelerating voltage of 10 kV and ~1.3 nA current. The secondary electron images in some cases allowed us to identify the location of the ion microprobe spot, which are shown in figures 7 through 13. The zircon zoning patterns are oscillatory and sector, which are consistent with igneous paragenesis (Cavosie and others, 2004). Individual grains are shades of yellow, black, blue, and/or green. These colors are primarily controlled by heavy rare earth elements $(REE)^{3+}$ (see for example, Marshall, 1988; Hanchar and Rudnick, 1995; Corfu and others, 2003). Trace amounts of Y^{3+}, Ti^{4+}, and U^{4+} can also result in yellow and blue CL emission (Hanchar and Rudnick, 1995). Radiation damage can quench CL (Poller and others, 2001; Corfu and others, 2003; Nasdala and others, 2003). Although it is difficult to determine the exact cause of CL in zircon, color CL imaging is a useful tool to understand possible changes in magmatic conditions as the grains crystallized. This

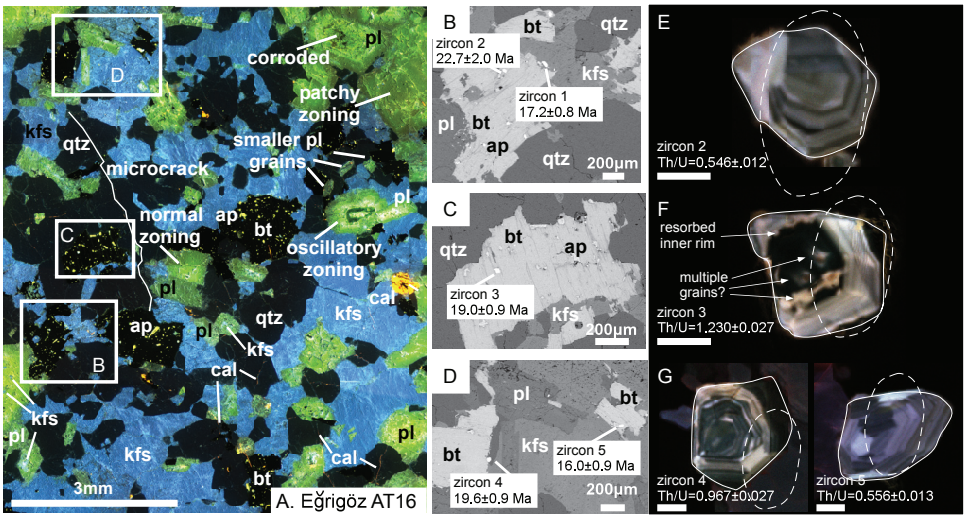

Fig. 8. (A) CL image of Eğrigöz sample AT16. Boxes indicate the locations of the BSE images in (B), (C), and (D). Ion microprobe $^{238}U/^{206}Pb$ ages ($\pm 1\sigma$) of the dated zircons are indicated. (E) CL image of the 22.7 ± 0.2 Ma zircon in panel (B). (F) CL image of the dated zircon in panel (C). (G) CL images of the dated zircons in panel (D). Scale bar for all zircon CL images is 10 µm. If possible, we indicate the location of the ion microprobe spot as a dashed oval.

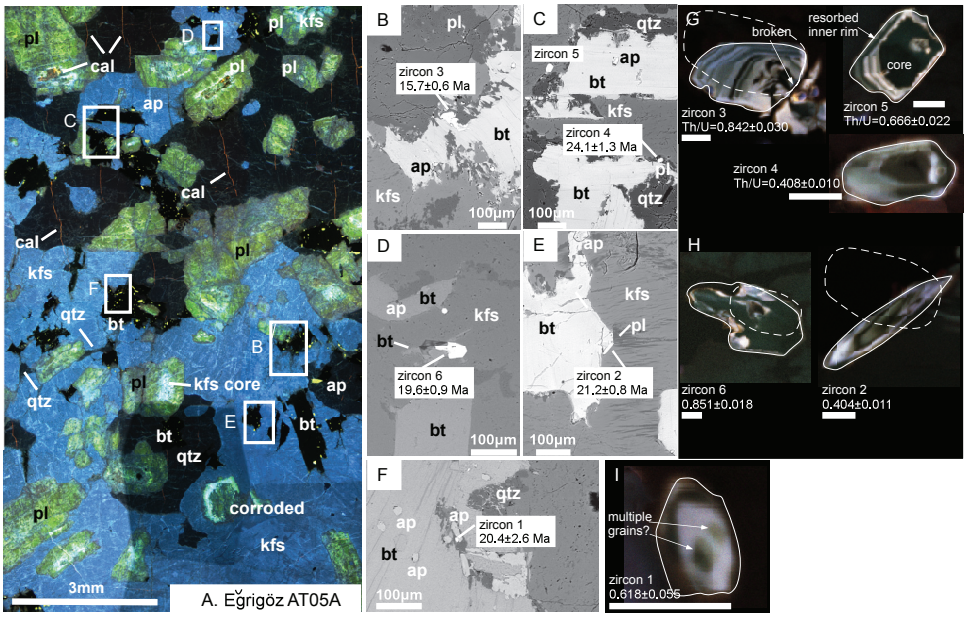

Fig. 9. (A) CL image of Eğrigöz sample AT05A. Boxes indicate the locations of the BSE images in (B), (C), (D), (E), and (F). Ion microprobe $^{238}U/^{206}Pb$ ages ($\pm 1\sigma$) of the dated zircons are indicated on the BSE images. (G) CL images of dated zircons in panels (B) and (C). (H) CL images of dated zircons in panels (D) and (E). (I) CL image of dated zircon in panel (F). Scale bar for all zircon CL images is 10 µm. If possible, we indicate the location of the ion microprobe spot as a dashed oval.

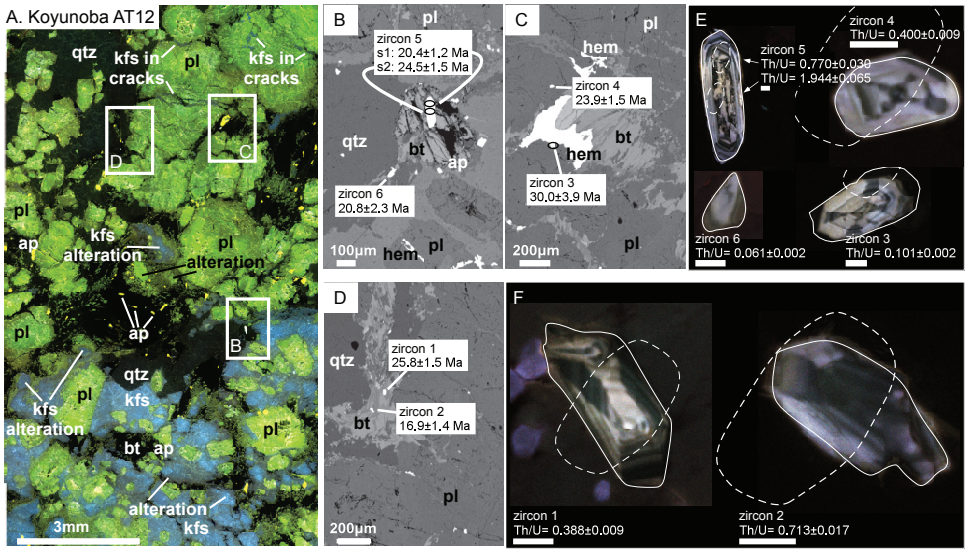

Fig. 10. (A) CL image of Koyunoba sample AT12. Boxes indicate the locations of the BSE images in (B), (C), and (D). Ion microprobe $^{238}U/^{206}Pb$ ages ($\pm 1\sigma$) of the dated zircons are indicated on the BSE images. (E) CL image of dated zircons in panel (B) and (C). (F) CL image of dated zircons in panel (D). Scale bar for all zircon CL images is 10 µm. If possible, we indicate the location of the ion microprobe spot as a dashed oval.

is the first time that color CL images of either rock thin sections or individual zircon grains have been reported for these plutons.

FIELD OBSERVATIONS

We targeted five specific contacts across the proposed Simav detachment, but only two of the five are exposed. The northern Eğrigöz pluton near sample AT02 (fig. 2) is bordered by skarn 10 to 100 meters thick (Oyman and others, 2012). This suggests no structure exists between the Eğrigöz pluton and the country rock it intruded at this location or the pluton post-dates any faulting. Near sample AT15 (fig. 2), a high angle normal fault, as evidenced by slickenlines and steps (strike 336°, dip 67° NE) was found along the border of the Eğrigöz pluton and the Simav graben. Note that the Simav detachment has an expected low dip angle (Işık and Tekeli, 2001). Near sample AT18, the western border of the Koyunoba pluton was covered by Neogene (Işık and others, 2003) volcanic tuff, therefore the existence of a detachment fault could not be determined.

GEOCHEMICAL RESULTS AND INTERPRETATIONS

Compositions of the Eğrigöz, Koyunoba, and Alaçam plutons range from granite to granodiorite on the total alkali ($Na_2O + K_2O$ wt.%) vs. silica (SiO_2) classification diagram (fig. 4A) (after Le Maitre and others, 1989; Wilson, 1989), with the exception of one Eğrigöz sample that is diorite (from Akay, 2009) and two of our northern samples are quartz monzonites (AT03 and AT04B). Silica content in these granitoids ranges from ~60 to 78 percent (fig. 4A).

The $Fe_2O_3/(Fe_2O_3 + MgO)$ vs. SiO_2 diagram (fig. 4B) can be used to understand the history of the magmatic source (Frost and others, 2001). Magnesian granitoids are typical of subduction zones because they are relatively oxidized during differentiation

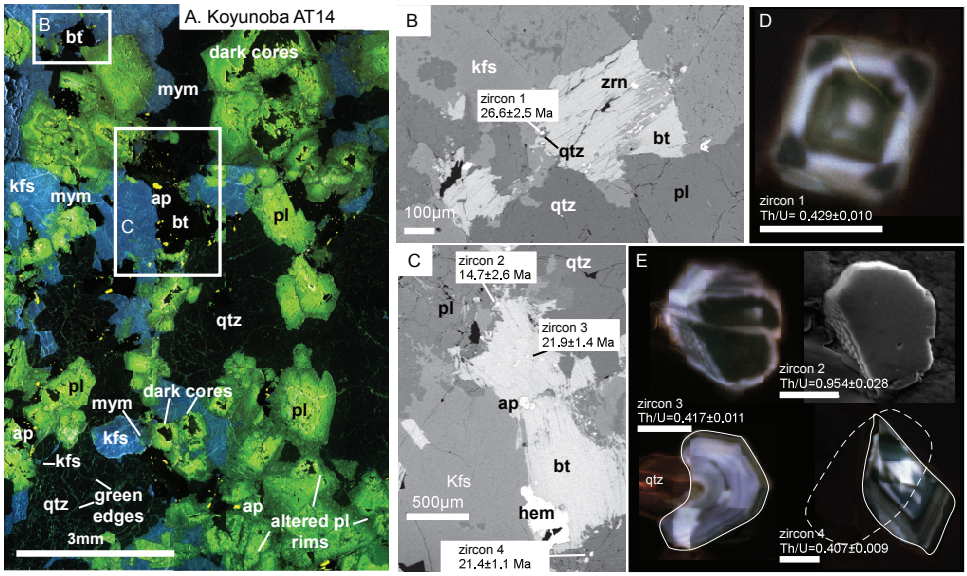

Fig. 11. (A) CL image of Koyunoba sample AT14. Abbreviations: "mym" = myrmekite. Boxes indicate the locations of the BSE images in (B) and (C). Ion microprobe $^{238}U/^{206}Pb$ ages ($\pm 1\sigma$) of the dated zircons are indicated on the BSE images. (D) CL image of dated zircon in panel (B). (E) CL images of dated zircons in panel (C). We also include a secondary electron image of zircon 2. Scale bar for all zircon CL images is 10 µm. If possible, we indicate the location of the ion microprobe spot as a dashed oval.

and ferroan granitoids source from anhydrous reduced magmas typical of extensional environments (Frost and Lindsley, 1991; Frost and others, 2001). In general, the plutons become more ferroan with increasing SiO_2 (fig. 4B). All of our Alaçam and Eğrigöz samples are magnesian, except two Eğrigöz rocks from the southeastern border of the pluton (WA10B and WA13). Most of our Koyunoba samples are ferroan, except three rocks (AT12, AT13, and AT17).

Using the Modified Alkali-Lime index (MALI, $Na_2O + K_2O - CaO$, Frost and others, 2001) the majority of samples are calc-alkalic. Only one of our northern Eğrigöz samples (AT02B) and four of our Koyunoba samples (AT09, AT10, AT11, and AT17) are alkali-calcic. Variations in this value are due to magmatic source and/or differentiation history (Frost and others, 2001). MALI numbers tend to become more alkalic as volcanic arc plutons show a decrease in continental crust contribution, likely because they are farther from a subduction zone (Frost and others, 2001). We find these plutons became more alkalic as they increase in SiO_2 (fig. 4C). Plutons containing both calc-alkalic and alkali-calcic samples suggest magma mixing because fractional crystallization of the melt should trend parallel to the boundaries of the MALI indices (Frost and Frost, 2008).

All our samples from the plutons described in this paper are peraluminous using the aluminum-saturation index [ASI, $Al/(Ca - 1.67P + Na + K)$] vs. SiO_2 (wt%) diagram (fig. 4D) (Frost and others, 2001), except northern Eğrigöz rocks AT04A, AT05A and AT05B and Alaçam sample AT21, which are metaluminous (ASI < 1 and molecular $Na + K < Al$). Peraluminous rocks have another aluminous phase present other than feldspar. These rocks have an ASI > 1 in cation proportions and may be formed from water-excess melting of mafic rocks.

Using the Rb vs. (Y + Nb) and Rb vs. (Yb + Ta) discrimination diagrams (fig. 5), all of the rocks collected by us are characteristic of a volcanic arc setting. Others have

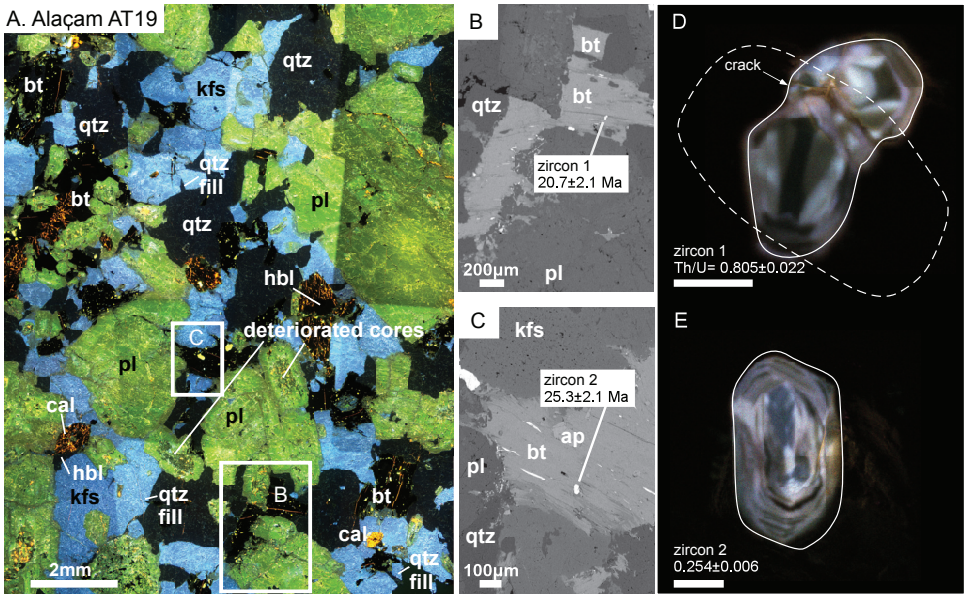

Fig. 12. (A) CL image of Alaçam sample AT19. Abbreviations: "mym" = myrmekite. Boxes indicate the locations of the BSE images in (B) and (C). Ion microprobe $^{238}U/^{206}Pb$ ages ($\pm 1\sigma$) of the dated zircons are indicated on the BSE images. (D) CL image of dated zircon in panel (B). (E) CL image of dated zircon in panel (C). Scale bar for all zircon CL images is 10 µm. If possible, we indicate the location of the ion microprobe spot as a dashed oval.

reported Eğrigöz samples that have trace elements consistent with syn-collisional or within plate granites (Özgenç and Ilbeyli, 2008; Akay, 2009). These discrepancies could be due to hydrothermal alteration, melting of host rocks during crystallization, magma mixing, depth of emplacement, and crystal settling, or the timing of plutonism relative to deformation events and tectonic setting. Rb can be mobilized during hydrothermal fluid alteration events (Mukasa and Henry, 1990) and lead to invalid interpretations.

The Eğrigöz, Koyunoba, and Alaçam plutons have similar chondrite-normalized rare earth element (REE) and trace element patterns (fig. 6). The samples are light REE enriched and many show negative Eu anomalies due to the fractional crystallization of plagioclase under reducing conditions (figs. 6A-C) (Rollinson, 1993). Zircon concentrates heavy REE over light REE, thus zircon fractionation enriches magmas in light REE and depletes in Zr. Sr values relative to chondrite indicate plagioclase fractionation, whereas Ba is controlled by the crystallization of K-feldspar. P is likely depleted due to the crystallization of apatite and/or monazite in some samples, and crystallization of titanite and/or rutile is likely responsible for the Ti depletion (figs. 6D-F).

GEOCHRONOLOGY AND CL

Results from the Eğrigöz Pluton

Samples WA12B, AT16, and AT05A were collected from the southern, central, and northern portions of the Eğrigöz pluton (table 1) and have major element compositions similar to those of plutons inboard of Cordilleran-type batholiths (magnesian, calc-alkalic; Frost and others, 2001).

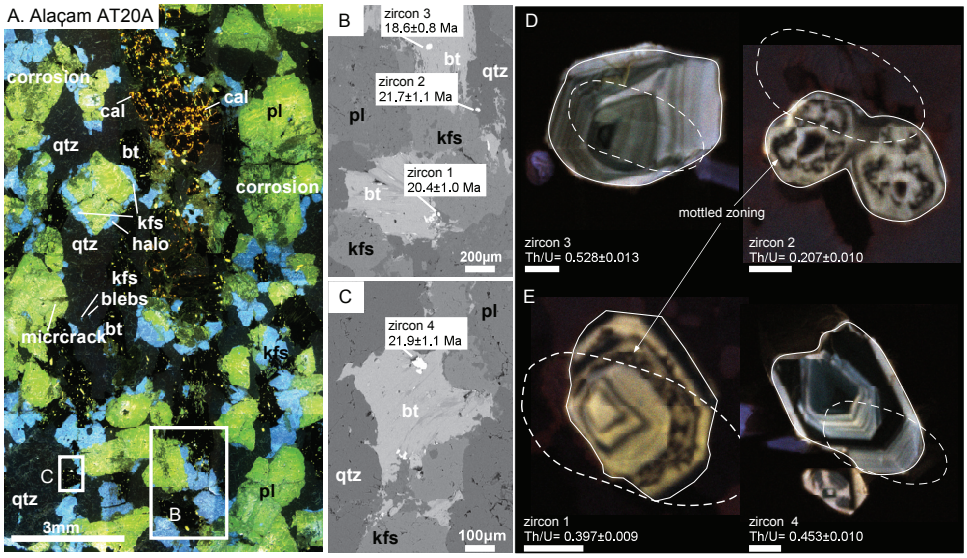

Fig. 13. (A) CL image of Alaçam sample AT20A. Boxes indicate the locations of the BSE images in (B) and (C). Ion microprobe $^{238}U/^{206}Pb$ ages ($\pm 1\sigma$) of the dated zircons are indicated on the BSE images. (D) CL image of dated zircons in panel (B). (E) CL image of dated zircons in panels (B) (left grain) and (C) (right grain). Scale bar for all zircon CL images is 10 μm. If possible, we indicate the location of the ion microprobe spot as a dashed oval.

Southern Eğrigöz sample WA12B.—Sample WA12B from the southern portion of the Eğrigöz pluton contains plagioclase of a range of grain sizes (1-3 mm) and zoning types (fig. 7A). The plagioclase grains are generally retrogressed with a mottled texture and patchy green to red rims. They are surrounded by K-feldspar, quartz, and/or biotite. Higher amounts of Ca are responsible for bright yellow-green CL in plagioclase (Catlos and others, 2011). Red-rimmed feldspars and microcrack boundaries are indicative of post-crystallization oxidation from fluid alteration (Finch and Klein, 1999). This process may have also created the red "flame-type" structures within some K-feldspar grains. Corroded cores in some plagioclase may be relic crystals from previous magmas (fig. 7A) (Janoušek and others, 2000). Some microcracks are blunted at these relic grain boundaries and may have acted as conduits for fluids to infiltrate cores and replace plagioclase with muscovite by metasomatism (Kretz and others, 1989). Plagioclase crystals may also contain small inclusions of K-feldspar, which suggests the reaction:

$$2CaAl_2Si_2O_8 + 2K^+ + 2H^+ \rightarrow KAlSiO_4 + 2Ca^{2+} + KAl_3Si_3O_{10}(OH)_2 \quad (4)$$

plagioclase + (potassium ions + hydrogen ions)$_{\text{in solution}}$ $\rightarrow$

K-feldspar + (calcium ions)$_{\text{in solution}}$ + muscovite.

The presence of fluids is clearly documented in the textures of the rock, including healed fluid inclusion planes and hydrous mineral precipitation within several microcracks. Large intergranular microcracks crosscut the rock and likely formed during post-crystallization deformation. Brittle deformation textures are also indicated by broken plagioclase grains, many of which are in close association with biotite (figs. 7A and 7C). Earlier ductile deformation microstructures are evidenced by grain-boundary migration of quartz into brownish-green plagioclase. Myrmekite is rare, but is found

TABLE 7

Ion microprobe $^{238}U/^{206}Pb$ data from zircons from the Eğrigöz pluton[a]

Zrn#[b]	$^{238}U/^{206}Pb$ Age (Ma) ±1σ[c]		^{206}Pb*% ±1σ[d]	$^{206}Pb/^{238}U$ ±1σ (x10^{-3})[e]	Th/U ±1σ[f]	UO^+/U^+ ±1σ[g]
			Sample WA12B			
z5[c]	22.3±1.1	22.2±1.1	96.6±0.4	3.463±0.177	0.616±0.013	8.078±0.022
z3	21.4±1.3	21.2±1.3	87.7±0.9	3.322±0.203	1.390±0.030	7.829±0.041
z4	20.3±0.7	21.4±0.9	66.3±1.6	3.161±0.111	0.726±0.016	10.20±0.036
z2	19.3±1.1	18.9±1.1	97.7±1.0	2.991±0.167	0.357±0.009	8.128±0.051
z1	19.0±1.4	17.2±1.3	68.4±2.5	2.952±0.217	1.422±0.097	8.279±0.140
			Sample AT16			
z2	22.7±2.0	18.7±3.7	14.6±0.8	3.525 ±0.316	0.546±0.012	7.485±0.038
z4	19.6±0.9	18.1±0.9	92.1±1.4	3.043 ±0.146	0.967±0.027	8.416±0.029
z3	19.0±0.9	18.2±0.8	79.8±1.5	2.956 ±0.134	1.230±0.027	8.854±0.046
z1	17.2±0.8	17.6±0.8	81.7±1.1	2.666 ±0.119	0.559±0.013	8.773±0.053
z5	16.0±0.9	15.6±1.3	67.9±1.5	2.461 ±0.133	0.556±0.013	8.426±0.038
			Sample AT05A			
z4[c]	24.1±1.3	24.7±1.4	84.7±0.6	3.771±0.201	0.408±0.010	7.993±0.020
z2	21.2±0.8	20.9±1.4	60.6±2.2	3.289±0.196	0.404±0.011	10.32±0.056
Z1	20.4±2.6	17.4±6.2	26.1±2.6	3.166±4.106	0.618±0.055	7.761±0.068
z6[c]	19.6±0.9	19.7±0.9	97.1±0.4	3.044 ±0.140	0.851±0.018	8.342±0.020
z3	15.7±0.6	19.1±0.7	78.4±1.0	2.434 ±0.092	0.842±0.030	9.188±0.060

[a] See table 11 for a summary of these results.
[b] Nomenclature is zircon grain number. Only 1 ion microprobe spot was placed on each grain.
[c] Reported $^{238}U/^{206}Pb$ age. The first age was calculated using ^{206}Pb correction assuming common $^{206}Pb/^{204}Pb = 18.86$, whereas the second age applies a ^{204}Pb correction using the measured ^{204}Pb.
[d] Percent radiogenically derived ^{206}Pb.
[e] Measured ratio in sample corrected for common Pb and instrument drift. See text for discussion for how ages are calculated.
[f] Relative to zircon standard 91500. See text for discussion for how this ratio is calculated.
[g] Measured ratio in sample. Ideally the UO^+/U^+ of the dated zircon lies within the range defined by the calibration curve, which ranged from 7.028 ± 0.014 to 8.634 ± 0.045.

along biotite and K-feldspar grain boundaries. Apatite and zircon grains are primarily clustered within biotite, a common texture in granitic assemblages potentially related to crystal settling (Ward and others, 1992; Bea, 1996).

Five zircon grains sample WA12B (fig. 7) yield Early Miocene $^{238}U/^{206}Pb$ ages that range from 22.3 ± 1.1 Ma to 19.0 ± 1.4 Ma, with a weighted mean age of 20.4 ± 0.5 Ma and Mean Square Weighted Deviation (MSWD) of 1.36 (figs. 7 and 14A; tables 7 and 11). Note that in most cases, the $^{235}U/^{207}Pb$ ages of these grains yield large errors; we attribute this to ion microprobe detection limits in measuring small amounts of radiogenic ^{207}Pb. The grain with the oldest $^{238}U/^{206}Pb$ age yields a meaningful $^{235}U/^{207}Pb$ age of 22.9 ± 2.9 Ma (table 10). All of the dated zircons are inclusions within or in contact with biotite grains and the zircon saturation temperature for this sample is ~788 °C (table 4) (Watson and Harrison, 1983).

To help interpret the results, we obtained CL images of the dated grains. These images show the zircons as blue, yellow, green, and/or black. Zircons included in a common biotite grain have blue rims (fig. 7E), but differ in their core colors. Two of the dated zircon grains have patchy green cores and two have distinctive yellow cores (figs. 7E and 7G). The change in color may be related to changing magmatic conditions as the grain crystallized (Hanchar and Rudnick, 1995). Grains with the green color have higher Th/U contents than the other dated zircons (figs. 7E and 7F). One large zircon grain is largely green and has a light blue inclusion, likely K-feldspar (fig. 7F). The oldest grain is yellow and black, has a small, cracked core, and shows

TABLE 8

Ion microprobe $^{238}U/^{206}Pb$ data from zircons from the Koyunoba pluton[a]

Zrn#[b]	$^{238}U/^{206}Pb$ Age (Ma) ±1σ[c]		^{206}Pb*% ±1σ[d]	$^{206}Pb/^{238}U$ ±1σ ($x10^{-3}$)[e]	Th/U ±1σ[f]	UO^+/U^+ ±1σ[g]
			Sample AT12			
Z3_s1	30.0±3.9	38.1±4.8	6.4±0.8	4.667 ±0.616	0.101±0.002	8.815±0.042
Z1_s1	25.8±1.5	24.0±1.8	59.8±1.2	4.003 ±0.234	0.388±0.009	7.933±0.029
Z5_s2	24.5±1.5	25.3±1.4	88.7±2.8	3.801 ±0.239	1.994±0.065	7.976±0.020
Z4_s1	23.9±1.5	22.2±1.8	59.6±1.4	3.710 ±0.237	0.400±0.009	7.814±0.024
Z6_s1	20.8±2.3	21.3±2.5	42.0±3.2	3.229 ±0.361	0.061±0.002	8.087±0.034
Z5_s1	20.4±1.2	22.0±1.2	89.1±1.7	3.171 ±0.183	0.770±0.030	7.978±0.051
Z2_s1	16.9±1.4	19.8±2.7	20.1±1.2	2.624 ±0.217	0.713±0.017	7.969±0.033
			Sample AT14			
Z1_s1	26.6±2.5	27.3±2.9	61.2±1.5	4.141±0.389	0.429±0.010	7.127±0.042
Z3_s1	21.9±1.4	21.0±1.6	73.7±1.9	3.400±0.220	0.417±0.011	7.896±0.048
Z4_s1	21.4±1.1	21.1±1.1	95.6±0.4	3.324±0.168	0.407±0.009	8.100±0.022
Z2_s1	14.7±2.6	2.3±6.2	8.0±1.4	2.275±0.410	0.954±0.028	11.34±0.15

[a] See table 11 for a summary of these results.
[b] Nomenclature is zircon grain number_ion microprobe spot number.
[c] Reported $^{238}U/^{206}Pb$ age. The first age was calculated using ^{206}Pb correction assuming common $^{206}Pb/^{204}Pb = 18.86$, whereas the second age applies a ^{204}Pb correction using the measured ^{204}Pb.
[d] Percent radiogenically derived ^{206}Pb.
[e] Measured ratio in sample corrected for common Pb and instrument drift. See text for discussion for how ages are calculated.
[f] Relative to zircon standard 91500. See text for discussion for how this ratio is calculated.
[g] Ideally the UO^+/U^+ of the dated zircon lies within the range defined by the calibration curve, which ranged from 7.028 ± 0.014 to 8.634 ± 0.045.

oscillatory zoning, typical of igneous crystallization (fig. 7G) (see for example, Corfu and others, 2003). The youngest zircon is small (~10 μm) with patchy zoning and is dominated by a blue color (fig. 7E).

Middle Eğrigöz sample AT16.—Sample AT16 was collected ~15 km north of sample WA12B in the middle of the Eğrigöz pluton and shows largely similar textures (figs. 2 and 8). This rock also contains apatite and zircon concentrated within biotite grains. K-feldspar is more abundant than plagioclase. Plagioclase grains of different sizes show a range of zoning types including normal (high-Ca cores and lower-Ca rims), patchy, and oscillatory zoning (fig. 8A). Some plagioclase cores are corroded. Cross-cutting relationships of microcracks within quartz and feldspars document brittle deformation. Small intergrowths and cores of K-feldspar within plagioclase suggest alteration was aided by hydrothermal fluids (Drake and others, 2008; Morad and others, 2010). Unlike WA12B, sample AT16 has calcite-filled microcracks within quartz and feldspar grains. We also do not see as many red-brown plagioclase rims, evidence for grain boundary migration, and myrmekite is absent.

Five zircon grains from sample AT16 yield Miocene $^{238}U/^{206}Pb$ ages ranging from 22.7 ± 2.0 Ma to 16.0 ± 0.9 Ma, with a weighted mean age of 20.8 ± 0.4 Ma and a MSWD of 15 (figs. 8 and 14A, tables 7 and 11). The MSWD indicates the ages are inconsistent with a single population. Similar to sample WA12B, this rock has a zircon saturation temperature of ~774 °C (table 3) and the zircons are located within or adjacent to biotite.

Most of the individual dated zircon grains show oscillatory zoning in CL, indicative of igneous crystallization (Cavosie and others, 2004). The CL colors are yellow, black, and blue. The youngest zircon is dominated by a blue hue and is located within a biotite that has sharp grain boundaries, whereas the older grains are mostly yellow in

TABLE 9

Ion microprobe $^{238}U/^{206}Pb$ data from zircons from the Alaçam pluton[a]

Zrn#[b]	$^{238}U/^{206}Pb$ Age (Ma) $\pm1\sigma$[c]		^{206}Pb*% $\pm1\sigma$[d]	$^{206}Pb/^{238}U$ $\pm1\sigma(x10^{-3})$[e]	Th/U $\pm1\sigma$ [f]	UO^+/U^+ $\pm1\sigma$[f]
			Sample AT19			
Z2	25.3±1.5	25.2±1.5	81.2±0.5	3.936±0.236	0.254±0.006	7.821±0.052
Z1	20.7±2.1	19.3±2.4	56.3±1.5	3.209±0.321	0.805±0.022	7.000±0.029
			Sample AT20A			
Z2	21.7±1.1	22.8±1.4	45.7±1.0	3.377±0.173	0.207±0.010	8.335±0.039
Z4	21.9±1.1	21.9±1.1	98.9±0.2	3.395±0.174	0.453±0.010	8.049±0.011
Z1	20.4±1.0	20.9±1.1	95.0±0.4	3.170±0.163	0.397±0.009	8.079±0.014
Z3	18.6±0.8	18.9±0.8	96.0±0.5	2.887±0.121	0.528±0.013	8.614±0.013
			Sample AT20B			
Z1	17.5±0.9	17.3±0.9	99.9±0.7	2.720±0.139	1.801±0.038	8.177±0.035

[a] See table 11 for a summary of these results.
[b] Nomenclature is zircon grain number. Only 1 ion microprobe spot was placed on each grain.
[c] Reported $^{238}U/^{206}Pb$ age. The first age was calculated using a ^{206}Pb correction assuming common $^{206}Pb/^{204}Pb = 18.86$, whereas the second age applies a ^{204}Pb correction using the measured ^{204}Pb.
[d] Percent radiogenically derived ^{206}Pb.
[e] Measured ratio in sample corrected for common Pb and instrument drift. See text for discussion for how ages are calculated.
[f] Relative to zircon standard 91500. See text for discussion for how this ratio is calculated.
[g] Ideally the UO^+/U^+ of the dated zircon lies within the range defined by the calibration curve, which ranged from 7.028 ± 0.014 to 8.634 ± 0.045.

color and are located near or within subhedral biotite grains (fig. 8). One grain has what appears to be multiple, euhedral zircon grains within its core and a partially resorbed inner rim (fig. 8F). This zircon has the highest Th/U of all of the dated grains

TABLE 10

Ion microprobe $^{235}U/^{207}Pb$ data from zircons from all plutons

Sample#_Zrn#[a]	$^{235}U/^{207}Pb$ Age (Ma) $\pm1\sigma$[b]	^{207}Pb*% $\pm1\sigma$[c]	$^{235}U/^{207}Pb$ $\pm1\sigma(x10^{-3})$[d]
	Eğrigöz pluton		
WA12B_Z5	22.9±2.9	62.2±4.7	22.80±2.37
AT05A_Z4	21.9±3.4	21.9±3.0	21.80±3.43
AT05A_Z6	17.6±1.9	62.7±5.9	17.44±1.95
	Koyunoba		
AT14_Z1	21.7±2.5	55.3±4.7	21.60±2.55
	Alaçam		
AT19_Z2	22.7±3.9	17.8±2.7	22.59±3.93
AT20A_Z1	14.2±2.0	42.2±5.2	14.13±2.00
AT20A_Z3	11.0±1.9	44.0±7.3	10.93±1.92
AT20A_Z4	19.5±1.3	82.4±2.8	19.40±1.23
AT20B_Z1	18.7±2.4	98.6±11.7	18.55±2.44

[a] Nomenclature is sample number zircon grain number spot number.
[b] Reported $^{235}U/^{207}Pb$ age. All ages calculated ^{206}Pb correction assuming common $^{206}Pb/^{204}Pb = 18.86$.
[c] Percent radiogenically derived ^{207}Pb.
[d] Measured ratio in sample corrected for common Pb and instrument drift. See text for discussion for how ages are calculated.

TABLE 11

Summary of $^{238}U/^{206}Pb$ ion microprobe ages

	Average age (±1σ)[a]	Weighted Mean Age (±1σ)[b]	MSWD[c]
	Eğrigöz		
WA12B	20.5±1.1	20.4±0.5	1.36
AT16	18.9±1.2	20.8±0.4	15.0
AT05A	20.2±1.4	20.8±0.4	21.3
All samples	19.9±1.3	20.7±0.2	10.4
	Koyunoba		
AT12	23.2±2.1	26.0±0.6	12.4
AT14	21.1±2.0	20.6±0.8	4.1
All samples	22.4±2.1	24.1±0.5	6.6
	Alaçam		
AT19	23.0±1.8	21.7±0.9	9.3
AT20A	20.6±1.0	21.0±0.5	3.0
All samples	21.4±1.4	21.7±0.4	4.7

[a] Average age of the dated zircons calculated assuming equal weight to each error.
[b] Weighted mean age, calculated using standard statistical methods with the precision of uncertainty taken into account.
[c] MSWD = mean square weighted deviation, an estimate of the weighted mean age being consistent with a single population.

in this rock. The youngest zircon is reversely discordant (fig. 14A), likely due to an overcorrection in the amount of common Pb.

Northern Eğrigöz sample AT05A.—Sample AT05A was collected from the most northern part of the Eğrigöz pluton and contains plagioclase grains significantly more altered than the other samples (figs. 2 and 9). This rock contains a large K-feldspar grain that envelopes quartz, biotite, and smaller corroded plagioclase grains (fig. 9A). Plagioclase grains are affected by swarms of microcracks and are commonly altered to K-feldspar (bright blue) and/or calcite (orange), suggesting carbonate-rich fluids affected the rock. Veins within deteriorated plagioclase are filled with K-feldspar. These veins likely acted as conduits to facilitate the alteration (Morad and others, 2010). Calcite is located in cores of deteriorated plagioclase and also fills microcracks within quartz and K-feldspar. Quartz fills microcracks that link plagioclase and/or biotite grains. Some biotite grains are surrounded by haloes of quartz (figs. 9C and 9F). Similar to the other Eğrigöz rocks, apatite and zircon grains are concentrated in or near biotite.

Four zircon grains from the sample AT05A yield Late Oligocene to Middle Miocene $^{238}U/^{206}Pb$ ages from 24.1 ± 1.3 Ma to 15.7 ± 0.6 Ma, with a weighted mean age of 20.8 ± 0.4 Ma and a MSWD of 21.3 (figs. 9 and 14, tables 7 and 11). Two of the dated grains yield meaningful Miocene $^{235}U/^{207}Pb$ ages, consistent with their $^{238}U/^{206}Pb$ ages (table 10). Although most of the CL images of the dated zircons show oscillatory zoning, one grain shows a mainly dark color in CL and has a Th/U of 0.851 ± 0.018 (zircon 6, fig. 9H). Two of the grains show evidence of possible smaller zircon inclusion(s) within their cores (zircons 1 and 5, figs. 9G and 9I). One of these grains did not yield a meaningful age (zircon 5) and also shows a resorbed inner rim (fig. 9G), whereas the other is reversely discordant (fig. 14A). The youngest zircon grain has a broken edge and is largely blue in CL, a color typical of the youngest zircon

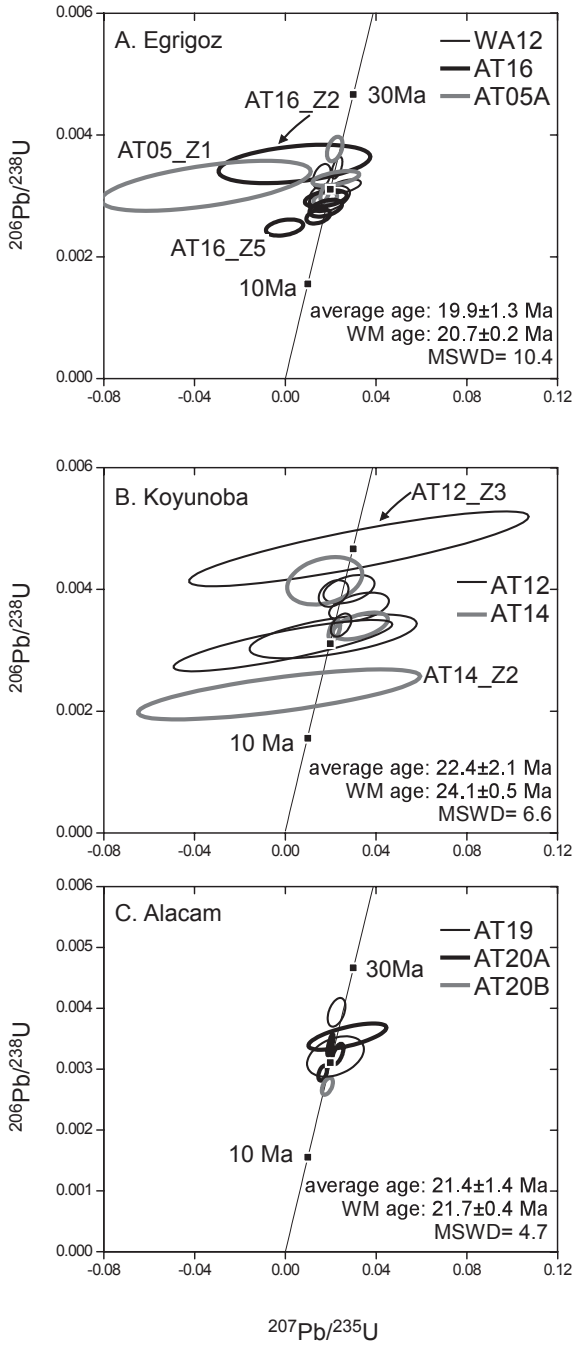

Fig. 14. Concordia diagrams of the zircons dated in the (A) Eğrigöz, (B) Koyunoba, and (C) Alaçam granitoids. We identify some individual analyses by sample number and "z." The $^{238}U/^{206}Pb$ average age, weighted mean age, and MSWD of all of the zircon ages ($\pm 1\sigma$) are indicated in the lower right corner of each concordia diagram. See tables 7–11 for analytical details.

grains dated in the Eğrigöz pluton. This sample has a zircon saturation temperature of ~780 °C (table 2), similar to other Eğrigöz rocks.

Results from the Koyunoba Pluton

Samples AT12 and AT14 were collected from the eastern edge and northern portion of the Koyunoba pluton, respectively (table 1 and fig. 2). Sample AT12 is similar to the Eğrigöz rocks as it has a major element composition similar to those of plutons inboard of Cordilleran-type batholiths (magnesian, calc-alkalic). However, sample AT14 appears to have a two-mica granite, A-type signature (ferroan, calc-alkalic; Frost and others, 2001).

Eastern edge Koyunoba sample AT12.—Sample AT12 has a cumulate texture and shows evidence of fluid alteration (figs. 2 and 10). K-feldspar is commonly altered in color along grain boundaries and microcracks. The mineral is often consumed by plagioclase and fills microcracks in larger plagioclase grains. As seen in the Eğrigöz samples, coarse-grained apatite and zircon are commonly included in biotite grains. This rock consists of plagioclase grains of different sizes with multiple generations of microcracks and veins filled with K-feldspar and quartz. At least two generations of plagioclase are present: one of large, patchy bright green grains, and a second of brown grains that consume K-feldspar and existing plagioclase.

Six zircon grains from sample AT12 range have Early Oligocene to Early Miocene $^{238}U/^{206}Pb$ ages from 30.0 ± 3.9 Ma to 16.9 ± 1.4 Ma, with a weighted mean age of 26.0 ± 0.6 Ma and a MSWD of 12.4 (figs. 10 and 14, tables 8 and 11). The oldest dated zircon (grain 3) is yellow in CL and is surrounded by iron oxide within a biotite grain (figs. 10C and 10E), whereas the youngest grain (zircon 2) has a bluish hue and is an inclusion in biotite (figs. 10D and 10F). The oldest grain and one nearby (zircon 4) shows oscillatory zoning in CL with dark bands that parallel crystal edges. The zircon grains with the lowest Th/U are found in this rock, including an Oligocene (zircon 3, 0.101 ± 0.002) and Late Miocene grains (zircon 6, 0.061 ± 0.002). We were able to place two on microprobe spots on one Miocene grain that has a complex, patchy core and oscillatory-zoned rim (zircon 5) (fig. 10E). The spot that yields the older age of this zircon has a much higher Th/U content than that of the younger age (1.944 ± 0.065 vs. 0.770 ± 0.030). The rock records a lower zircon saturation temperature than the Eğrigöz samples of ~762 °C (table 5).

Northern Koyunoba sample AT14.—Sample AT14 was collected from the northern edge Koyunoba pluton, closest to the proposed Simav detachment (figs. 2 and 11). CL images reveal coarse-grained subhedral plagioclase grains with altered edges and large K-feldspar and quartz grains. Myrmekite is common at both K-feldspar and plagioclase grain boundaries. Some plagioclase phenocrysts have dark deteriorated cores filled with muscovite. Apatite and zircon are found near biotite grains, as is typical of the imaged granitoids. Grain boundaries in quartz appear bright green, suggesting the presence of small veins of plagioclase. K-feldspar is also seen as filling microcracks along grain boundaries in quartz (fig. 11A).

Four zircon grains were dated from sample AT14 and yield Late Oligocene to Miocene ages (26.6 ± 2.5 Ma to 14.7 ± 2.6 Ma), with a weighted mean age of 20.6 ± 0.8 Ma and a MSWD of 4.1 (figs. 11 and 14, tables 8 and 11). These ages are consistent with the results from other samples in the field area. The oldest grain is within a quartz inclusion in biotite and shows a blue and black pattern in CL consistent with its symmetry (fig. 11D). This grain also yields a meaningful $^{235}U/^{207}Pb$ age of 21.7 ± 2.5 Ma (table 10). The youngest grain is also blue and is located at the edge of a biotite grain. The CL image of this grain shows a distinctive crack, although it is not visible in the secondary electron image likely because it has annealed or healed (fig. 11E). Radiation damage in zircon can heal over geologic time at temperatures >200 to 250 °C (for example, Nasdala and others, 2001). The Th/U content of this grain is

high compared to the other older zircons (0.954 ± 0.028 vs. ~0.407-0.429) (fig. 11; table 8). The biotite that contains the young grain also has bluish zircon inclusions that are 21.9 ± 1.4 Ma and 21.4 ± 1.1 Ma with igneous oscillatory zoning (figs. 11C and 11E). This rock records the highest zircon saturation temperature of any of the dated rocks of ~805 °C (table 5).

Results from the Alaçam Pluton and Crosscutting Volcanic Rock

Samples AT19 and AT20A were collected from the Alaçam pluton (fig. 2 and table 1) and have major element compositions similar to those of plutons inboard of Cordilleran-type batholiths (magnesian, calc-alkalic, Frost and others, 2001). We also dated a single zircon from sample AT20B, which is from a hydrothermally altered rhyolite dike within the Alaçam pluton at the same location as AT20A (see table 1 for mineral assemblage). This rock was dated to constrain the timing of the latest stage of igneous activity.

Alaçam sample AT19.—Sample AT19 has calcite located in cores of plagioclase, quartz veins, and along cleavage cracks in hornblende (figs. 2 and 12A). Plagioclase grains of multiple sizes have cracked and deteriorated cores filled with muscovite and calcite. Microcracks through plagioclase grains likely acted as conduits for fluid to enter the cores. Quartz also fills grain boundaries and microcracks within K-feldspar. Apatite and zircon grains are concentrated within biotite grains as is typical of these granitoids.

We only dated two zircons grains from sample AT19, which are 25.3 ± 1.5 Ma and 20.7 ± 2.1 Ma (fig. 12; table 9). Both grains are concordant (fig. 14C) and the young grain also yields a meaningful $^{235}U/^{207}Pb$ age of 22.7 ± 3.9 Ma (table 10). These zircons show black and blue colors and oscillatory zoning in CL (figs. 12D and 12E). The youngest zircon is located within a biotite and appears to have been cracked and recrystallized along a cleavage plane (figs. 12B and 12D). The crack is filled with material that shows an orange color in CL. The ion microprobe spot was placed on a dark core in this portion of the grain that yields a much higher Th/U content than the other dated zircon (0.805 ± 0.022 vs. 0.254 ± 0.006). The zircon saturation temperature of this rock is ~778 °C (table 6).

Sample AT20A.—Sample AT20A was collected ~0.6 km northwest of sample AT19 (fig. 2) and contains large altered plagioclase grains locally surrounded by K-feldspar (fig. 13A). In some places, corrosion textures exist within plagioclase grains evidenced by alteration of the mineral to darker green. Microcracks are abundant and appear to have been conduits for fluid alteration. Many smaller plagioclase grains are surrounded by K-feldspar halos. Orange calcite is located within cleavage planes and microcracks within biotite grains. Quartz microfractures are filled with small K-feldspar blebs. Sample AT20A also contains abundant apatite and zircon, again, located primarily adjacent or within biotite grains.

Four zircons from sample AT20A were dated and have $^{238}U/^{206}Pb$ ages that range from 21.9 ± 1.1 Ma to 18.6 ± 0.8 Ma with a weighted mean age of 21.0 ± 0.5 Ma and MSWD of 3 (figs. 13 and 14, tables 9 and 11). The oldest grain is located within a biotite grain and shows blue and black colors and oscillatory zoning in CL. This grain also yields a $^{235}U/^{207}Pb$ age of 19.5 ± 1.3 Ma (table 10). A distinctive mottled zoning pattern is seen in two yellow and black zircon grains (figs. 13D and 13E). The spots that overlapped this mottled pattern yield much lower Th/U contents than grains that show oscillatory zoning (figs. 13D and 13E). One of the zircons with a mottled mid-rim yields a $^{235}U/^{207}Pb$ age of 14.2 ± 2.0 Ma (grain 1), whereas the youngest zircon in the rock is an inclusion in biotite and has a $^{235}U/^{207}Pb$ age of 11.0 ± 1.9 Ma (grain 3, table 10). The grain is bluish in CL and shows oscillatory zoning. Sample AT20A records a zircon saturation temperature of ~786 °C (table 6).

Volcanic sample AT20B.—Sample AT20B (fig. 2) from the rhyolite dike contains biotite and subhedral plagioclase phenocrysts in a groundmass of K-feldspar and quartz. Accessory minerals are scarce but some zircons are found concentrated near biotite grains and within the groundmass. We dated a single zircon grain from sample AT20B, which yields a $^{238}U/^{206}Pb$ age of 17.5 ± 0.9 Ma ($^{235}U/^{207}Pb$ age is 18.7 ± 2.4 Ma; table 10). This grain has the highest Th/U of any of the dated grains (1.801 ± 0.038; table 9).

DISCUSSION

Data

The majority (~80%) of the reported compositions of the Northern Menderes Massif granitoids indicate they are magnesian, calc-alkalic and peraluminous granite to granodiorites. Magnesian granites are typical of subduction zones whereas ferroan granites are typical of extensional environments (Frost and Lindsley, 1991; Frost and others, 2001). Many of the Northern Menderes Massif granitoids are similar geochemically to plutons in the main portion of the Corderilla, such as the Northern Idaho batholith (Frost and others, 2001), although variations in their chemistry exist (figs. 4-6). The range of compositions have been reported for the Eğrigöz, Koyunoba, and Alaçam plutons (Özgenç and Ilbeyli, 2008; Dilek and others, 2009; Ilbeyli and Kibici, 2009; Akay, 2009) likely reflects heterogeneities caused by magma mixing, partial melting, crustal contamination, and post-emplacement fluid interactions. We suggest that the presence of both may be a result of a change from compression to extension in the Aegean region and multiple sources for the origin of these rocks.

Although the granitoids imaged and dated here were collected from fresh outcrops, fluid-rock interaction is evidenced in all samples by the variation of CL colors along grain boundaries and microcracks, patchy zoning within feldspars, chemical alteration of plagioclase grains, and the presence of calcite precipitated in microcracks, and muscovite in deteriorated plagioclase cores. Different grain sizes and zoning patterns of plagioclase, corroded relic cores, and "flame-type" structures within K-feldspar are evidence of magma mixing (Janoušek and others, 2000; Salisbury and others, 2008; Catlos and others, 2011).

Zircon grains in all of the northern Menderes granitoids are found only near, in contact with, or adjacent to biotite grains. This textural relationship indicates that zircon was likely unstable in the quartzofeldspathic portion of the rock and accumulated as biotite crystallized (Watt and others, 1996). We do not see significant differences in zircon saturation temperatures for any of the compositions for these plutons, which average 782 ± 12 °C.

Overall, the granites contain zircon grains that overlap in age. They crystallized over a ~15 m.y. time frame, predominantly centered ~20 Ma (table 11). The length of time is not unusual; continual generation of magmas in a mantle wedge is possible even after the cessation of subduction (Harris and others, 1994). The plutons may have started to crystallize as early as the Oligocene and were exhumed by the Middle Miocene. The results indicate the proposed Simav detachment does not separate rocks of widely differing ages and that, instead, the three plutons should be treated as a unit in terms of their Oligo-Miocene exhumation history. More fieldwork is required to discern the precise location and role of this proposed structure in exhuming these rocks, as in many places it is not evident (near samples AT02-AT08, near sample AT18, fig. 2). The volcanic zircon from a sample that crosscuts the Alaçam pluton, data from low temperature thermochronometers (Thomson and Ring, 2006), and the young $^{235}U/^{207}Pb$ ages of some zircons (table 10) suggest the plutons were nearing the surface by the Middle to Late Miocene.

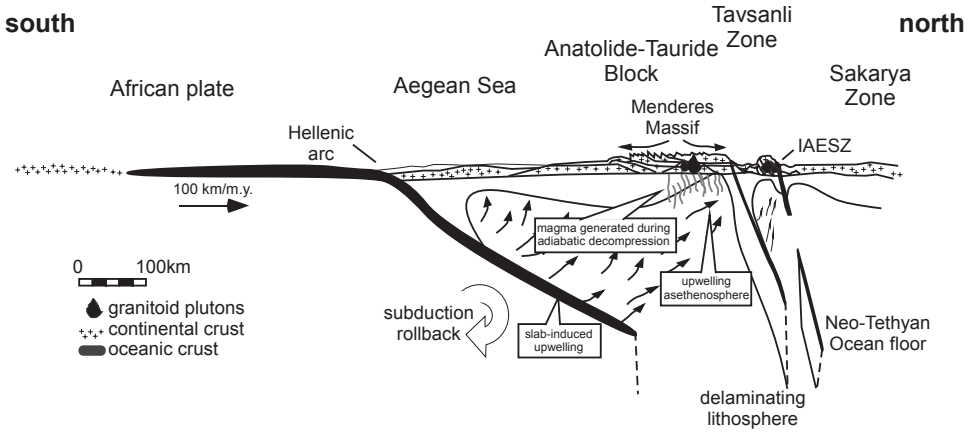

Fig. 15. Lithospheric-scale cartoon cross-section of the Aegean region showing potential sources for the Northern Menderes Massif granitoids and their tectonic environment. The time frame for the cross-section is Late Oligocene to Early Miocene. The subduction zone cartoon is adapted from Cloos and others (2005). Scale is a rough approximation. Western Turkey is modeled as a region of stacked subduction zones that operated at different times. During the Early to Late Cretaceous, the Tavşanlı Zone develops. During the Eocene, granitoid arc magmas from the northern edge of the Anatolide-Tauride block intrude the Tavşanlı Zone. During the Oligocene this slab breaks off that allows adiabatic decompression melting in Tavşanlı lithospheric mantle. The Hellenic Arc experiences ongoing subduction and is also a source for the Northern Menderes granites. See text for further discussion.

We note that the older Oligocene to Early Miocene zircons typically show a yellow color in CL and younger Late Miocene grains are often characterized by a blue hue (for example, fig. 8). A change in color in CL of the zircon grain likely reflects a change in magmatic composition (Hanchar and Rudnick, 1995). We saw no clear correlations between Th/U and zircon age, color or zoning pattern, although higher Th/U ratios are typically shown by zircons with black or dark green colors in CL (figs. 7-9) and the Alacam zircon grains with mottled yellow zoning patterns have lower Th/U contents than those without these patterns (fig. 13). All zircons have Th/U contents consistent with igneous crystallization (>0.1) (Cavosie and others, 2004), except a single 10 μm–sized 20.8 ± 2.3 Ma grain from the Alacam pluton (0.061 ± 0.002).

Model

We suggest the Eğrigöz, Koyunoba, and Alaçam plutons were emplaced in a regime dominated by extension following the collision of the Anatolide-Tauride Block with the Tavşanlı Zone. Figure 15 is a lithospheric-scale cross-section of western Anatolia during the Late Oligocene to Early Miocene from the Sarkaya zone in the north to the African plate in the south. The region is shown as an amalgamation of stacked subduction zones that operated at different times. The Menderes Massif is located south of the Tavşanlı Zone, which is characterized by HP/LT assemblages intruded by Eocene-Oligocene age granitoids (for example, the Orhaneli, Topuk, Göynükbelen, and Tepeldağ plutons; Harris and others, 1994; Delaloye and Bingöl, 2000; Whitney and others, 2011). The Tavşanlı Zone is bound to the north by the İzmir-Ankara-Erzincan Suture Zone, which marks the closure of a branch of the Neo-Tethyan ocean and the division of rocks of Laurasian affinity in the north (for example, Sarkaya zone) from those associated with Gondwana to the south (for example, Anatolide-Tauride block) (Okay, 1984; Okay and others, 1998; Okay, 2008; Moix and others, 2008). This suture formed largely during the Eocene (see for

example, Moix and others, 2008) but the Tavşanlı Zone is characterized by Late Cretaceous subduction metamorphism (see for example, Sherlock and others, 1999; Whitney and others, 2011). The Menderes Massif is located south of the Tavşanlı Zone and is currently experiencing large-scale extension likely due to the roll back of the African slab along the Hellenic arc (see for example, ten Veen and Postma, 1999; Laigl and others, 2004; Dhont and others, 2006; Bonev and Beccaletto, 2007; Dilek and Sandvol, 2009).

Figure 15 shows possible sources for the generation of Northern Menderes Massif granitoids in the back arc setting (see also Flower and others, 2001), which include simple slab induced upwelling, adiabatic decompression as the northern edge of the Anatolide-Tauride block delaminates, and upwelling asthenosphere as the continental lithosphere thins during extension. It is possible that a slab of negative buoyancy (oceanic) located on the northern edge of the Anatolide-Tauride block delaminates and magma migrates into the northern portion of the Menderes Massif during the Oligocene to Late Miocene. Recent mantle tomography shows the potential for slab tear and hot asthenospheric upwelling just south of the field area in the Kula region (Biryol and others, 2011). However, we speculate that a primary source of these rocks is partial melting of the subducting African plate and overlying lower-middle crust of the Eurasian plate (for example, Dilek and others, 2009), although other sources exist, including the decompression melts and contributions from upwelling asthenosphere (Alici and others, 2002; Tokçaer and others, 2005). Our data show that the Northern Menderes Massif granites have a range of sources.

Zircon ages are consistent with the magmatism largely propagating from the north to the south in the Aegean region (also shown by Dilek and Altunkaynak, 2007; Jolivet and Brun, 2010). Monazite ages from granites located ~150 km south of our rocks in the central Menderes Massif are Middle Miocene (15.0 ± 2.8; Salihli granodiorite, 15.0 ± 1.7 Ma; Turgutlu granodiorite; Catlos and others, 2010). Zircon from intrusions in the Naxos metamorphic core complex to the southwest are 15.4 to 11.3 Ma (Keay and others, 2001), whereas those from Mykonos are 13.5 ± 0.3 Ma (Brichau and others, 2008). Mylonitic orthogneisses related to the initial stage of a metamorphic core complex formation from Serifos are 15 to 11 Ma (Rb-Sr ages) (Iglseder and others, 2009). K-feldspars from mylonitic augen gneisses from the South Cyclades Shear Zone on the Greek island of Ios experienced an episode of argon loss ~14 Ma, likely due to a thermal pulse coincident to and related to the intrusion of magmas (Baldwin and Lister, 1998). These timing constraints suggest extension has propagated from north to south during the Oligocene to Miocene in the Aegean region (Dilek and Altunkaynak, 2007; Jolivet and Brun, 2010). This may be the result of a combination of slowing subduction along the Hellenic arc and the development of extensional structures in these core complexes.

The method employed here, correlating *in situ* ion microprobe geochronology, major and trace element whole rock geochemistry, with CL imaging at both the grain- and thin section–scales is a powerful method for deciphering tectonomagmatic history of Northern Menderes Massif granitoids, and could be applied in similar ways to other similar settings both in Turkey and elsewhere. The data and observations provide key information regarding the timing pluton emplacement, their exhumation, and complex fluid history.

ACKNOWLEDGMENTS

This material is based upon work supported by the National Science Foundation under Grant No. 0937254. Additional funding was provided by the Jackson School of Geosciences. Samples were obtained with the help of Drs. Yasar Kibici, Ibrahim Cemen, and Mehmet Demirbilek and students Okan Yildiz, Ozge Karaman, and Esra Yalcin. Comments from Drs. Mark Cloos, Dan Barker, Stuart Thomson, and Seth

Kruckenberg, greatly improved the original manuscript. The authors thank the UCLA National Ion Microprobe Facility (particularly Drs. Rita Economos and Axel Schmitt), which is partially supported by funding from the National Science Foundation's Instrumentation and Facilities Program. Ages were obtained with the help of Jackson School students Kathryn Huber and Tim Shin. Thin section scale CL imagery was generated with the support of the Smithsonian Institution's National Museum of Natural History Fellowship program. Some figures were drafted with the assistance of Karen Black.

References

Agostini, S., Doglioni, C., Innocenti, F., Manetti, P., and Tonarini, S., 2010, On the geodynamics of the Aegean Rift, *in* Çemen, I., editor, Extensional tectonics in the Basin and Range, the Aegean, and western Anatolia: Tectonophysics, v. 488, n. 1–4, p. 7–21, http://dx.doi.org/10.1016/j.tecto.2009.07.025

Akay, E., 2009, Geology and petrology of the Simav magmatic complex (NW Anatolia) and its comparison with the Oligo-Miocene granitoids in NW Anatolia; implications on Tertiary tectonic evolution of the region: International Journal of Earth Sciences, v. 98, n. 7, p. 1655–1675, http://dx.doi.org/10.1007/s00531-008-0325-0

Akdeniz, N., and Konak, N., 1979, Menderes Masifinin simav dolayindaki kayabirimleri ve metabazik, metaultramafik kayalarin konomu: Bulletin of the Geological Society of Turkey, v. 22, p. 175–183 [in Turkish].

Alici, P., Temel, A., and Gourgaud, A., 2002, Pb-Nd-Sr isotope and trace element geochemistry of Quaternary extension-related alkaline volcanism; a case study of Kula region (western Anatolia, Turkey): Journal of Volcanology and Geothermal Research, v. 115, n. 3–4, p. 487–510, http://dx.doi.org/10.1016/S0377-0273(01)00328-6

Altunkaynak, Ş., Dilek, Y., Genç, C. Ş., Sunal, G., Gertisser, R., Furnes, H., Foland, K. A., and Yang, J., 2012, Spatial, temporal and geochemical evolution of Oligo-Miocene granitoid magmatism in western Anatolia, Turkey: Gondwana Research, v. 21, n. 4, p. 961–986, http://dx.doi.org/10.1016/j.gr.2011.10.010

Baldwin, S. L., and Lister, G. S., 1998, Thermochronology of the South Cyclades shear zone, Ios, Greece: Effects of ductile shear in the argon partial retention zone: Journal of Geophysical Research, v. 103, n. B4, p. 7315–7336, http://dx.doi.org/10.1029/97JB03106

Bea, F., 1996, Residence of REE, Y, Th and U in granites and crustal protoliths; Implications for the chemistry of crustal melts: Journal of Petrology, v. 37, n. 3, p. 521–552, http://dx.doi.org/10.1093/petrology/37.3.521

Bingöl, E., Delaloye, M., and Ataman, G., 1982, Granitic intrusions in western Anatolia; a contribution to the geodynamic study of this area: Eclogae Geologicae Helvetiae, v. 75, p. 437–446.

Biryol, C. B., Beck, S. L., Zandt, G., and Özacar, A. A., 2011, Segmented African lithosphere beneath the Anatolian region inferred from teleseismic *P*-wave tomography: Geophysical Journal International, v. 184, n. 3, p. 1037–1057, http://dx.doi.org/10.1111/j.1365-246X.2010.04910.x

Bonev, N., and Beccaletto, L., 2007, From syn- to post-orogenic Tertiary extension in the north Aegean region: constraints on the kinematics in the eastern Rhodope-Thrace, Bulgaria-Greece and the Biga Peninsula, NW Turkey, *in* Taymaz, T., Yilmaz, Y., and Dilek, Y., editors, The geodynamics of the Aegean and Anatolia: Geological Society, London, Special Publications, v. 291, p. 113–142, http://dx.doi.org/10.1144/SP291.6

Bozkurt, E., Satir, M., and Buğdaycioğlu, Ç., 2011, Surprisingly young Rb/Sr ages from the Simav extensional detachment fault zone, northern Menderes Massif, Turkey: Journal of Geodynamics, v. 52, n. 5, p. 406–431, http://dx.doi.org/10.1016/j.jog.2011.06.002

Boztug, D., Harlavan, Y., Jonckheere, R., Can, I., and Sari, R., 2009, Geochemistry and K-Ar cooling ages of the Ilıca, Cataldag (Balıkesir) and Kozak (Izmir) granitoids, west Anatolia, Turkey: Geological Journal, v. 44, n. 1, p. 79–103, http://dx.doi.org/10.1002/gj.1132

Brichau, S., Ring, U., Carter, A., Bolhar, R., Monie, P., Stockli, D., and Brunel, M., 2008, Timing, slip rate, displacement and cooling history of the Mykonos detachment footwall, Cyclades, Greece, and implications for the opening of the Aegean Sea basin: Journal of the Geological Society, London, v. 165, n. 1, p. 263–277, http://dx.doi.org/10.1144/0016-76492006-145

Buick, I. S., 1991, The late-Alpine evolution of an extensional shear zone, Naxos, Greece: Journal of the Geological Society, London, v. 148, n. 1, p. 93–103, http://dx.doi.org/10.1144/gsjgs.148.1.0093

Burkut, Y., 1966, Kuzeybati Anadolu'da Yer Alan Plutonlarin Mukayesli Jenetik Etudu: Istanbul, ITU Maden Fak, Yayini, p. 272 [in Turkish].

Catlos, E. J., Baker, C., Sorensen, S. S., Çemen, I., and Hancer, M., 2010, Geochemistry, geochronology, and cathodoluminescence imagery of the Salihli and Turgutlu granites (central Menderes Massif, western Turkey): Implications for Aegean tectonics: Tectonophysics, v. 488, n. 1–4, p. 110–130, http://dx.doi.org/10.1016/j.tecto.2009.06.001

Catlos, E. J., Baker, C. B., Sorensen, S. S., Jacob, L., and Çemen, I., 2011, Linking microcracks and mineral zoning of detachment-exhumed granites to their tectonomagmatic history: Evidence from the Salihli and Turgutlu plutons in western Turkey (Menderes Massif): Journal of Structural Geology, v. 33, n. 5, p. 951–969, http://dx.doi.org/10.1016/j.jsg.2011.02.005

Cavosie, A. J., Wilde, S., Liu, D., Weiblen, P. W., and Valley, J. W., 2004, Internal zoning and U-Th-Pb

chemistry of Jack Hills detrital zircons: a mineral record of early Archean to Mesoproterozoic (4348-1576 Ma) magmatism: Precambrian Research, v. 135, n. 4, p. 251–279, http://dx.doi.org/10.1016/j.precamres.2004.09.001

Çemen, I., Catlos, E. J., Gogus, O., and Ozerdem, C., 2006, Post-collisional extensional tectonics and exhumation of the Menderes Massif in the Western Anatolia Extended Terrane, Turkey, *in* Dilek., Y., and Pavlides, S., editors, Postcollisional Tectonics and Magmatism in the Mediterranean Region and Asia: Geological Society of America Special Papers, v. 409, p. 353–379, http://dx.doi.org/10.1130/2006.2409(18)

Cloos, M., Sapiie, B., van Ufford, A. Q., Weiland, R. J., Warren, P. Q., and McMahon, T. P., 2005, Collisional delamination in New Guinea: The geotectonics of subducting slab breakoff: Geological Society of America Special Paper, v. 400, p. 1–51, http://dx.doi.org/10.1130/2005.2400

Compston, W., Williams, I. S., and Meyer, C., 1984, U-Pb geochronology of zircons from Lunar Breccia 73217 using a Sensitive High Mass-Resolution Ion Microprobe: Journal of Geophysical Research, v. 89, p. B525–B534, http://dx.doi.org/10.1029/JB089iS02p0B525

Coney, P. J., 1980, Cordilleran metamorphic core complexes: An overview, *in* Crittenden, M. D., Coney, P. J., and Davis, G. H, editors, Cordilleran metamorphic core complexes: Geological Society of America Memoirs, v. 153, p. 7–34.

Coney, P. J., and Harms, T. A., 1984, Cordilleran metamorphic core complexes: Cenozoic extensional relics of Mesozoic compression: Geology, v. 12, n. 9, p. 550–554, http://dx.doi.org/10.1130/0091-7613(1984)12⟨550:CMCCCE⟩2.0.CO;2

Corfu, F., Hanchar, J. M., Hoskin, P. W. O., and Kinny, P., 2003, Atlas of zircon textures: Reviews in Mineralogy and Geochemistry, v. 53, n. 1, p. 469–500, http://dx.doi.org/10.2113/0530469

Corti, G., Bonini, M., Conticelli, S., Innocenti, F., Manetti, P., and Sokoutis, D., 2003, Analogue modelling of continental extension: a review focused on the relations between the patterns of deformation and the presence of magma: Earth—Science Reviews, v. 63, n. 3–4, p. 169–247, http://dx.doi.org/10.1016/S0012-8252(03)00035-7

Cox, R. A., Dempster, T. J., Bell, B. R., and Rogers, G., 1996, Crystallization of the Shap Granite: evidence from zoned K-feldspar megacrysts: Journal of the Geological Society, London, v. 153, n. 4, p. 625–635, http://dx.doi.org/10.1144/gsjgs.153.4.0625

De St. Jorre, L., and Smith, D. G. W., 1988, Cathodoluminescent Gallium-enriched feldspars from the Thor Lake rare-metal deposits, Northwest Territories: Canadian Mineralogist, v. 26, p. 301–308.

Delaloye, M., and Bingöl, E., 2000, Granitoids from western and northwestern Anatolia; geochemistry and modeling of geodynamic evolution: International Geology Review, v. 42, n. 3, p. 241–268, http://dx.doi.org/10.1080/00206810009465081

Demirci, A., Bekler, T., and Ozden, S., 2012, The 19 May 2011 Simav Earthquake (Mw=5.8) and its aftershocks, Western Turkey: Source mechanisms and spectral source parameters: European Geosciences Union Geophysical Research Abstracts, v. 14, p. EGU2012-7539-1, 2012.

Denele, Y., Lecomte, E., Jolivet, L., Lacombe, O., Labrousse, L., Huet, B., and Le Pourhiet, L., 2011, Granite intrusion in a metamorphic core complex: The example of the Mykonos Laccolith (Cyclades, Greece): Tectonophysics, v. 501, n. 1–4, p. 52–70, http://dx.doi.org/10.1016/j.tecto.2011.01.013

Dhont, D., Chorowicz, J., and Luxey, P., 2006, Anatolian escape tectonics driven by Eocene crustal thickening and Neogene-Quaternary extensional collapse in the eastern Mediterranean region, *in* Dilek., Y., and Pavlides, S., editors, Postcollisional Tectonics and Magmatism in the Mediterranean Region and Asia: Geological Society of America Special Papers, v. 409, p. 441–462, http://dx.doi.org/10.1130/2006.2409(21)

Dilek, Y., and Altunkaynak, Ş., 2007, Cenozoic crustal evolution and mantle dynamics of post-collisional magmatism in western Anatolia: International Geology Review, v. 49, n. 5, p. 431–453, http://dx.doi.org/10.2747/0020-6814.49.5.431

Dilek, Y., and Sandvol, E., 2009, Seismic structure, crustal architecture and tectonic evolution of the Anatolian-African plate boundary and the Cenozoic orogenic belts in the eastern Mediterranean region, *in* Murphy, J. B., Keppie, J. D., and Hynes, A. J., editors, Ancient orogens and modern analogues: Geological Society, London, Special Publications, v. 327, p. 127–160, http://dx.doi.org/10.1144/SP327.8

Dilek, Y., Altunkaynak, S., and Oner, Z., 2009, Syn-extensional granitoids in the Menderes core complex and the late Cenozoic extensional tectonics of the Aegean province, *in* Ring, U., and Wernicke, B., editors, Extending a Continent: Architecture, Rheology and Heat Budget: Geological Society, London, Special Publications, v. 321, p. 197–223, http://dx.doi.org/10.1144/SP321.10

Dinter, D. A., and Royden, L., 1993, Late Cenozoic extension in northeastern Greece; Strymon Valley detachment system and Rhodope metamorphic core complex: Geology, v. 21, n. 1, p. 45–48, http://dx.doi.org/10.1130/0091-7613(1993)021⟨0045:LCEING⟩2.3.CO;2

Drake, H., Tullborg, E. L., and Annersten, H., 2008, Red-staining of the wall rock and its influence on the reducing capacity around water conducting fractures: Applied Geochemistry, v. 23, n. 7, p. 1898–1920, http://dx.doi.org/10.1016/j.apgeochem.2008.02.017

Erkül, F., 2010, Tectonic significance of synextensional ductile shear zones within the early Miocene Alaçamdağ granites, northwestern Turkey: Geological Magazine, v. 147, n. 4, p. 611–637, http://dx.doi.org/10.1017/S0016756809990719

Ersoy, Y. E., Helvacı, C., and Sözbilir, H., 2010, Tectono-stratigraphic evolution of the NE-SW-trending superimposed Selindi Basin: Implications for late Cenozoic crustal extension in western Anatolia, Turkey: Tectonophysics, v. 488, n. 1–4, p. 210–232, http://dx.doi.org/10.1016/j.tecto.2010.01.007

Faulds, J. E., Bouchot, V., Moeck, I., and Oguz, K., 2009, Structural controls on geothermal systems in western Turkey: A preliminary report: Geothermal Resources Council Transactions, v. 33, p. 375–381.

Faure, G., 1986, Principles of isotope geology: New York, John Wiley and Sons, 589 p.

Finch, A. A., and Klein, J., 1999, The causes and petrological significance of cathodoluminescence emissions from alkali feldspar: Contributions to Mineralogy and Petrology, v. 135, n. 2–3, p. 234–243, http://dx.doi.org/10.1007/s004100050509

Flower, M. F. J., Russo, R. M., Tamaki, K., and Hoang, N., 2001, Mantle contamination and the Izu-Bonin-Mariana (IBM) "high-tide mark": evidence for mantle extrusion caused by Tethyan closure: Tectonophysics, v. 333, n. 1–2, p. 9–34, http://dx.doi.org/10.1016/S0040-1951(00)00264-X

Frost, B. R., and Frost, C. D., 2008, A geochemical classification for feldspathic igneous rocks: Journal of Petrology, v. 49, n. 11, p. 1955–1969, http://dx.doi.org/10.1093/petrology/egn054

Frost, B. R., and Lindsley, D. H., 1991, Occurrence of iron-titanium oxides in igneous rocks: Reviews in Mineralogy, v. 25, n. 1, p. 433–468.

Frost, B. R., Barnes, C. G., Collins, W. J., Arculus, R. J., Ellis, D. J., and Frost, C. D., 2001, A geochemical classification of granitic rocks: Journal of Petrology, v. 42, n. 11, p. 2033–2048, http://dx.doi.org/10.1093/petrology/42.11.2033

Gautier, P., and Brun, J. P., 1994, Crustal-scale geometry and kinematics of late-orogenic extension in the central Aegean (Cyclades and Evvia Island): Tectonophysics, v. 238, n. 1–4, p. 399–424, http://dx.doi.org/10.1016/0040-1951(94)90066-3

Geake, J. E., Walker, G., Telfer, D. J., Mills, A. A., and Garlick, G. F. J., 1973, Luminescence of lunar, terrestrial, and synthesized plagioclase, caused by Mn^{2+} and Fe^{3+}: Geochimica et Cosmochimica Acta Supplement 4, Proceedings 4th Lunar Science Conference, v. 3, p. 3181–3189.

Genç, S. C., 1998, Evolution of the Bayramiç magmatic complex, northwestern Anatolia: Journal of Volcanology and Geothermal Research, v. 85, n. 1–4, p. 233–249, http://dx.doi.org/10.1016/S0377-0273(98)00057-2

Gessner, K., Piazolo, S., Güngör, T., Ring, U., Kröner, A., and Passchier, C., 2001, Tectonic significance of deformation patterns in granitoid rocks of the Menderes nappes, Anatolide Belt, Southwest Turkey: International Journal of Earth Sciences, v. 89, n. 4, p. 766–780, http://dx.doi.org/10.1007/s005310000106

Goetze, J., Krbetschek, M. R., Habermann, D., and Wolf, D., 2000, High-resolution cathodoluminescence studies of feldspar minerals, *in* Pagel, M., Barbin, V., Blanc, P., and Ohnenstetter, D., editors, Cathodoluminescence in Geosciences: Berlin, Springer, p. 245–270.

Görür, N., Oktay, F. Y., Seymen, İ., and Şengör, A. M. C., 1984, Paleotectonic evolution of Tuzgölü basin complex, Central Turkey: sedimentary record of a Neo-Tethyan closure, *in* Dixon, J. E., and Robertson, A. H. F., editors, The geological evolution of the eastern Mediterranean: Geological Society, London, Special Publications, v. 17, p. 467–482, http://dx.doi.org/10.1144/GSL.SP.1984.017.01.34

Hanchar, J., and Rudnick, R. L., 1995, Revealing hidden structures: The application of cathodoluminescence and back-scattered electron imaging to dating zircons from lower crustal xenoliths: Lithos, v. 36, n. 3–4, p. 289–303, http://dx.doi.org/10.1016/0024-4937(95)00022-4

Harris, N. B. W., Kelley, S., and Okay, A. I., 1994, Post-collision magmatism and tectonics in northwest Anatolia: Contributions to Mineralogy and Petrology, v. 117, n. 3, p. 241–252, http://dx.doi.org/10.1007/BF00310866

Hasözbek, A., Satır, M., Erdoğan, B., Akay, E., and Siebel, W., 2010, Early Miocene post-collisional magmatism in NW Turkey: geochemical and geochronological constraints: International Geology Review, v. 53, n. 9, p. 1098–1119, http://dx.doi.org/10.1080/00206810903579302

Hetzel, R. R., Ring, U., Akal, C., and Troesch, M., 1995, Miocene NNE-directed extensional unroofing in the Menderes Massif, southwestern Turkey: Journal of the Geological Society, London, v. 152, n. 4, p. 639–654, http://dx.doi.org/10.1144/gsjgs.152.4.0639

Hibbard, M. J., 1981, The magma mixing origin of mantled feldspars: Contributions to Mineralogy and Petrology, v. 76, n. 2, p. 158–170, http://dx.doi.org/10.1007/BF00371956

Howard, K. A., Wooden, J. L., Barnes, C. G., Premo, W. R., Snoke, A. W., and Lee, S. Y., 2011, Episodic growth of a Late Cretaceous and Paleogene intrusive complex of pegmatitic leucogranite, Ruby Mountains core complex, Nevada, USA: Geosphere, v. 7, n. 5, p. 1220–1248, http://dx.doi.org/10.1130/GES00668.1

Iglseder, C., Grasemann, B., Schneider, D. A., Petrakakis, K., Miller, C., Klötzli, U. S., Thöni, M., Zámolyi, A., and Rambousek, C., 2009, I and S-type plutonism on Serifos (W-Cyclades, Greece): Tectonophysics, v. 473, n. 1–2, p. 69–83, http://dx.doi.org/10.1016/j.tecto.2008.09.021

Ilbeyli, N., and Kibici, Y., 2009, Collision-related granite magma genesis, potential sources and tectonomagmatic evolution: comparison between central, northwestern and western Anatolia (Turkey): International Geology Review, v. 51, n. 3, p. 252–278, http://dx.doi.org/10.1080/00206810802673933

Işık, V., and Tekeli, O., 2001, Late orogenic crustal extension in the northern Menderes massif (western Turkey): evidence for metamorphic core complex formation: International Journal of Earth Sciences, v. 89, n. 4, p. 757–765, http://dx.doi.org/10.1007/s005310000105

Işık, V., Seyitoğlu, G., and Çemen, I., 2003, Ductile-brittle transition along the Alasehir detachment fault and its structural relationship with the Simav detachment fault, Menderes massif, western Turkey: Tectonophysics, v. 374, n. 1–2, p. 1–18, http://dx.doi.org/10.1016/S0040-1951(03)00275-0

Işık, V., Tekeli, O., and Seyitoğlu, G., 2004a, The $^{40}Ar/^{39}Ar$ age of extensional ductile deformation and granitoid intrusion in the northern Menderes core complex: Implications for the initation of extensional tectonics in western Turkey: Journal of Asian Earth Sciences, v. 23, n. 4, p. 555–566, http://dx.doi.org/10.1016/j.jseaes.2003.09.001

Işık, V., Gürsü, S., Göncüoğlu, C., and Seyitoğlu, G., 2004b, Deformational and geochemical features of syn-tectonic Koyunoba and Egrigoz granitoids, western Turkey: Thessaloniki, Greece, April 2004, 5th International Symposium on Eastern Mediterranean Geology Abstracts, Proceedings, v. 3, p. 1143–1146.

Janoušek, V., Bowes, D. R., Braithwaite, C. J. R., and Roger, G., 2000, Microstructural and mineralogical evidence for limited involvement of magma mixing in the petrogenesis of a Hercynian high-K

calc-alkaline instrusion: the Kozárovice granodiorite, Central Bohemian Pluton, Czech Republic: Transactions of the Royal Society of Edinburgh: Earth Sciences, v. 91, p. 15–26, http://dx.doi.org/10.1017/S0263593300007264
Jolivet, L., and Brun, J. P., 2010, Cenozoic geodynamic evolution of the Aegean: International Journal of Earth Sciences, v. 99, n. 1, p. 109–138, http://dx.doi.org/10.1007/s00531-008-0366-4
Jolivet, L. L., Daniel, J. M., Truffert, C., and Goffe, B., 1994, Exhumation of deep crustal metamorphic rocks and crustal extension in arc and back-arc regions: Lithos, v. 33, n. 1–3, p. 3–30, http://dx.doi.org/10.1016/0024-4937(94)90051-5
Jones, J. V., Connelly, J. N., Karlstrom, K. E., Williams, M. L., and Doe, M. F., 2009, Age, provenance, and tectonic setting of Paleoproterozoic quartzite successions in the southwestern United States: Geological Society of America Bulletin, v. 121, p. 247–264, http://dx.doi.org/10.1130/B26351.1
Kaya, 1972, Tavşanlı yöresi ofiyolit sorununun ana çizgileri: Türkiye Jeologi Kurumu Bülteni (Geological Society of Turkey Bulletin), v. 15, n. 1, p. 26–108 [in Turkish].
Keay, S., Lister, G., and Buick, I., 2001, The timing of partial melting, Barrovian metamorphism and granite intrusion in the Naxos metamorphic core complex, Cyclades, Aegean Sea, Greece, *in* Teyssier, C., and Vanderhaeghe, O., editors, Partial melting of crust and flow of orogens: Tectonophysics, v. 342, n. 3–4, p. 275–312.
Ketin, I., 1966, Tectonic units of Anatolia (Asia Minor): Bulletin of the Mineral Research and Exploration of Turkey, v. 66, p. 23–24.
Kilias, A. A., Fassoulas, C., and Mountrakis, D., 1994, Tertiary extension of continental crust and uplift of Psiloritis metamorphic core complex in the central part of the Hellenic Arc (Crete, Greece): Geologische Rundschau, v. 83, n. 2, p. 417–430, http://dx.doi.org/10.1007/BF00210555
Konak, N., 2002, Geological map of Turkey: Izmir Turkiye Jeoloji Haritasi, scale 1:500,000.
Kretz, R., Hartree, R., and Jones, P., 1989, Metasomatic crystallization of muscovite in granite and tourmaline in schist related to pegmatite emplacement near Yellowknife, Canada: Contributions to Mineralogy and Petrology, v. 102, n. 2, p. 191–204, http://dx.doi.org/10.1007/BF00375340
Laigle, M., Sachpazi, M., and Him, A., 2004, Variation of seismic coupling with slab detachment and upper plate structure along the western Hellenic subduction zone: Tectonophysics, v. 391, n. 1–4, p. 85–95, http://dx.doi.org/10.1016/j.tecto.2004.07.009
Le Maitre, R. W., Bateman, P., Dudek, A., Keller, J., Lameyre Le Bas, M. J., Sabine, P. A., Schmid, R., Sorensen, H., Streckeisen, A., Woolley, A. R., and Zanettin, B., 1989, A classification of igneous rocks and glossary of terms: Oxford, Blackwell Science, 193 p.
Lister, G. S., and Davis, G. A., 1989, The origin of metamorphic core complexes and detachment faults formed during Tertiary continental extension in the northern Colorado River region, U.S.A.: Journal of Structural Geology, v. 11, n. 1–2, p. 65–94, http://dx.doi.org/10.1016/0191-8141(89)90036-9
Ludwig, K. R., 2012, User's Manual for Isoplot 3.75: A Geochronological Toolkit for Microsoft Excel: Berkeley, California, Berkeley Geochronology Center Special Publication, v. 5, p. 47.
Mariano, A. N., and Ring, P. J., 1975, Europium-activated cathodoluminescence in minerals: Geochimica et Cosmochimica Acta, v. 39, n. 5, p. 649–660, http://dx.doi.org/10.1016/0016-7037(75)90008-3
Marshall, D. J., 1988, Cathodoluminescence of geological materials: Boston, Unwin Hyman, 146 p.
Meijer, P. Th., and Wortel, M. J. R., 1997, Present-day dynamics of the Aegean region: a model analysis of the horizontal pattern of stress and deformation: Tectonics, v. 16, n. 6, p. 879–895, http://dx.doi.org/10.1029/97TC02004
Moix, P., Beccaletto, L., Kozur, H. W., Hochard, C., Rosselet, F., and Stampfli, G. M., 2008, A new classification of the Turkish terranes and sutures and its implication for the paleotectonic history of the region: Tectonophysics, v. 451, n. 1–4, p. 7–39, http://dx.doi.org/10.1016/j.tecto.2007.11.044
Morad, S. S., El-Ghali, M. A. K., Caja, M. A., Sirat, M., Al-Ramadan, K., and Mansurbeg, H., 2010, Hydrothermal alteration of plagioclase in granitic rocks from Proterozoic basement of SE Sweden: Geological Journal, v. 45, n. 1, p. 105–116, http://dx.doi.org/10.1002/gj.1178
Mukasa, S. B., and Henry, D. J., 1990, The San Nicolás Batholith of coastal Peru: early Palaeozoic continental arc or continental rift magmatism?: Journal of the Geological Society, London, v. 147, p. 27–39, http://dx.doi.org/10.1144/gsjgs.147.1.0027
Nasdala, L., Wenzel, M., Vavra, G., Irmer, G., Wenzel, T., and Kober, B., 2001, Metamictisation of national zircon: Accumulation versus thermal annealing of radioactivity-induced damage: Contributions to Mineralogy and Petrology, v. 141, n. 2, p. 125–144, http://dx.doi.org/10.1007/s004100000235
Nasdala, L., Zhang, M., Kempe, U., Panczer, G., Gaft, M., Andrut, M., and Plotze, M., 2003, Spectroscopic methods applied to zircon: Reviews in Mineralogy and Geochemistry, v. 53, n. 1, p. 427–467, http://dx.doi.org/10.2113/0530427
Okay, A. I., 1984, Distribution and characteristics of the north-west Turkish blueschists, *in* Dixon, J. E., and Robertson, A. H. F., editors, The geological evolution of the eastern Mediterranean: Geological Society, London, Special Publications, v. 17, p. 455–466, http://dx.doi.org/10.1144/GSL.SP.1984.017.01.33
——— 1986, High-pressure/low-temperature metamorphic rocks of Turkey, *in* Evans, B. W., and Brown, E. H., editors, Blueschists and eclogites: Geological Society of America Memoirs, v. 164, p. 333–347.
——— 2008, Geology of Turkey: A synopsis: Anschnitt, v. 21, p. 19–42.
Okay, A. I., and Satır, M., 2000, Coeval plutonism and metamorphism in a latest Oligocene metamorphic core complex in northwest Turkey: Geological Magazine, v. 137, n. 5, p. 495–516, http://dx.doi.org/10.1017/S0016756800004532
Okay, A. I., Harris, N. B. W., and Kelley, S. P., 1998, Exhumation of blueschists along a Tethyan suture in northwest Turkey: Tectonophysics, v. 285, p. 275–299, http://dx.doi.org/10.1016/S0040-1951(97)00275-8
Orhan, A., Seyrek, E., and Tosun, H., 2007, A probabilistic approach for earthquake hazard assessment of

the Province of Eskisehir, Turkey: Natural Hazards and Earth System Science, v. 7, p. 607–614, http://dx.doi.org/10.5194/nhess-7-607-2007

Oyman, T., Özgenç, I., Tokcaer, M., and Akbulut, M., 2012, Petrology, geochemistry and evolution of the iron skarns along the northern contact of the Egrigoz plutonic complex, western Anatolia, Turkey: Turkish Journal of Earth Sciences, v. 21, p. 1–41, doi:10.3906/yer-1006-2.

Özburan, M., and Gürer, O. F., 2011, Late Cenozoic polyphase deformation and basin development, Kütahya region, western Turkey: International Geology Review, http://dx.doi.org/10.1080/00206814.2011.644108.

Özgenç, I., and Ilbeyli, N., 2008, Petrogenesis of the Late Cenozoic Egrigöz pluton in western Anatolia, Turkey: Implications for magma genesis and crustal processes: International Geology Review, v. 50, n. 4, p. 375–391, http://dx.doi.org/10.2747/0020-6814.50.4.375

Özgenç, I., and Oyman, T., 2004, Skarn-gossan mineralisation in the roof-pendants of the Egrigoz Granitoid (western Turkey); preliminary results, *in* Cook, N. J., and Ciobanu, C. L., editors, Gold-silver-telluride deposits of the Golden Quadrilateral, south Apuseni Mts., Romania; guidebook of the International field workshop of IGCP Project 486: International Association on the Genesis of Ore Deposit Guidebook Series 12, p. 249–250.

Parsons, I., Steele, D. A., Lee, M. R., and Magee, C. W., 2008, Titanium as cathodoluminescence activator in alkali K-feldspar: American Mineralogist, v. 93, n. 5–6, p. 875–879, http://dx.doi.org/10.2138/am.2008.2711

Pearce, K. A., Harris, N. B. W., and Tindle A. G., 1984, Trace element discrimination diagrams for tectonic interpretation of granitic rocks: Journal of Petrology, v. 25, n. 4, p. 956–983, http://dx.doi.org/10.1093/petrology/25.4.956

Poller, U., Hugh, J., Hoppe, P., and Williams, I. S., 2001, REE, U, Th, and Hf distribution in zircon from western Carpathian Variscan granitoids: a combined cathodoluminescence and ion microprobe study: American Journal of Science, v. 301, n. 10, p. 858–876, http://dx.doi.org/10.2475/ajs.301.10.858

Ramseyer, K. K., Al Dahan, A. A., Collini, B., and Landström, O., 1992, Petrological modifications in granitic rocks from the Siljan impact structure; evidence from Cathodoluminescence: Tectonophysics, v. 216, n. 1–2, p. 195–204, http://dx.doi.org/10.1016/0040-1951(92)90166-4

Ring, U., and Collins, A. S., 2005, U-Pb SIMS dating of synkinematic granites; timing of core-complex formation in the northern Anatolide Belt of western Turkey: Journal of the Geological Society, London, v. 162, n. 2, p. 289–298, http://dx.doi.org/10.1144/0016-764904-016

Ring, U., Johnson, C., Hetzel, R., and Gessner, K., 2003, Tectonic denudation of a Late Cretaceous–Tertiary collisional belt: regionally symmetric cooling patterns and their relation to extensional faults in the Anatolide belt of western Turkey: Geological Magazine, v. 140, p. 421–441, http://dx.doi.org/10.1017/S0016756803007878

Rollinson, H. R., 1993, Using Geochemical Data; Evaluation, Presentation, Interpretation: United Kingdom, Longman Scientific and Technical, 352 p.

Salisbury, M. J., Bohrson, W. A., Clynne, M. A., Ramos, F. C., and Hoskin, P., 2008, Multiple plagioclase crystal populations identified by crystal size distribution and *in situ* chemical data: Implications for timescales of magma chamber processes associated with the 1915 eruption of Lassen Peak, CA.: Journal of Petrology, v. 49, n. 10, p. 1755–1780, http://dx.doi.org/10.1093/petrology/egn045

Schneider, D. A., Edwards, M. A., Kidd, W. S. F., Zeitler, P. K., and Coath, C. D., 1999, Early Miocene anatexis identified in the western syntaxis, Pakistan Himalaya: Earth and Planetary Science Letters, v. 167, n. 3–4, p. 121–129, http://dx.doi.org/10.1016/S0012-821X(99)00022-9

Scott, J. M., Palin, J. M., Cooper, A. F., Sagar, M. W., Allibone, A. H., and Tulloch, A. J., 2011, From richer to poorer: zircon inheritance in Pomona Island Granite, New Zealand: Contributions to Mineralogy and Petrology, v. 161, n. 5, p. 667–681, http://dx.doi.org/10.1007/s00410-010-0556-5

Senel, M., and Aydal, N., 2002, Geological Map of Turkey (Izmir and Istanbul sheets): Maden Tetkik ve Arama Genel Mudurlugu, Eskisehir Yolu, Turkey, scale 1:500,000.

Şengör, A. M. C., and Yılmaz, Y., 1981, Tethyan evolution of Turkey: A plate tectonic approach: Tectonophysics, v. 75, n. 3–4, p. 181–241, http://dx.doi.org/10.1016/0040-1951(81)90275-4

Şengör, A. M. C., Yılmaz, Y., and Ketin, İ., 1980, Remnants of a pre-Late Jurassic ocean in northern Turkey: Fragments of Permian-Triassic Paleo-Tethys?: Geological Society of America Bulletin, v. 91, n. 10, p. 599–609, http://dx.doi.org/10.1130/0016-7606(1980)91⟨599:ROAPJO⟩2.0.CO;2

Seyitoğlu, G., 1997, The Simav Graben: An example of young E-W trending structures in the Late Cenozoic extensional system of Western Turkey: Turkish Journal of Earth Sciences, v. 6, p. 135–141.

Seyitoğlu, G., and Scott, B. C., 1996, The cause of N-S extensional tectonics in western Turkey: Tectonic escape vs back-arc spreading vs orogenic collapse: Journal of Geodynamics, v. 22, n. 1–2, p. 145–153, http://dx.doi.org/10.1016/0264-3707(96)00004-X

Seyitoğlu, G., Işık, V., and Çemen, I., 2004, Complete Tertiary exhumation history of the Menderes Massif, western Turkey: an alternative working hypothesis: Terra Nova, v. 16, n. 6, p. 358–364, http://dx.doi.org/10.1111/j.1365-3121.2004.00574.x

Sherlock, S., Kelley, S., Inger, S., Harris, N., and Okay, A., 1999, ^{40}Ar-^{39}Ar and Rb-Sr geochronology of high-pressure metamorphism and exhumation history of the Tavşanlı Zone, NW Turkey: Contributions to Mineralogy and Petrology, v. 137, n. 1–2, p. 46–58, http://dx.doi.org/10.1007/s004100050581

Siivola, J., and Schmid, R., 2007, Classification and nomenclature scheme; list of mineral abbreviations, *in* Fettes, D., and Desmons, J., editors, Metamorphic rocks, a classification and glossary of terms; recommendations of the International Union of Geological Sciences Subcommission on the Systematics of Metamorphic Rocks: Cambridge, United Kingdom, University Press Cambridge, p. 93–110.

Sorensen, S., Harlow, G. E., and Rumble III, D., 2006, The origin of jadeitite-forming subduction-zone fluids: CL-guided SIMS oxygen-isotope and trace-element evidence: American Mineralogist, v. 91, n. 7, p. 979–996, http://dx.doi.org/10.2138/am.2006.1949

Steiger, R. H., and Jäger, E., 1977, Subcommission on geochronology: Convention on the use of decay constants in geo- and cosmochronology: Earth and Planetary Science Letters, v. 36, n. 3, p. 359–362, http://dx.doi.org/10.1016/0012-821X(77)90060-7

Stirling, D., Duncan, A. M., Guest, J. E., and Finch, A. A., 1999, Petrogenesis of plagioclase phenocryst of Mount Etna, Sicily, with particular reference to the 1983 eruption: contribution from cathodoluminescence petrography: Mineralogical Magazine, v. 63, n. 2, p. 189–199, http://dx.doi.org/10.1180/002646199548420

Sun, S. S., and McDonough, W. F., 1989, Chemical and isotopic systematics of oceanic basalts: implications for mantle composition and processes. Magmatism in ocean basins: Geological Society, London, Special Publications, v. 42, p. 313–345, http://dx.doi.org/10.1144/GSL.SP.1989.042.01.19

Tekeli, O., Işık, V., Seyitoğlu, G., and Çemen, I., 2001, The $^{40}Ar/^{39}Ar$ age of ductile extension and granitoid intrusions in the northern Menderes massif, western Turkey: Adana, Turkey, Fourth International Turkish Geology Symposium, Abstracts, p. 226.

ten Veen, J. H., and Postma, G., 1999, Roll-back controlled vertical movements of outer-arc basins of the Hellenic subduction zone, (Crete, Greece): Basin Research, v. 11, n. 3, p. 243–266, http://dx.doi.org/10.1046/j.1365-2117.1999.00098.x

Thomson, S. N., and Ring, U., 2006, Thermochronologic evaluation of postcollision extension in the Anatolide Orogen, western Turkey: Tectonics, v. 25, TC3005, http://dx.doi.org/10.1029/2005TC001833

Tokçaer, M., Agostini, S., and Savaşçin, M. Y., 2005, Geotectonic setting and origin of the youngest Kula volcanics (Western Anatolia), with a new emplacement model: Turkish Journal of Earth Sciences, v. 14, p. 145–166.

Ulusay, R., Tuncay, E., Sonmez H., and Gokceoglu, C., 2004, An attenuation relationship based on Turkish strong motion data and iso-acceleration map of Turkey: Engineering Geology, v. 74, n. 3–4, p. 265–291, http://dx.doi.org/10.1016/j.enggeo.2004.04.002

Vandenberg, L. S., and Lister, G. S., 1996, Structural analysis of basement tectonites from the Aegean metamorphic core complex of Ios Cyclades, Greece: Journal of Structural Geology, v. 18, n. 12, p. 1437–154, http://dx.doi.org/10.1016/S0191-8141(96)00068-5

Ward, C. D., McArthur, J. M., and Walsh, J. N., 1992, Rare earth element behaviour during evolution and alteration of the Dartmoor Granite, SW England: Journal of Petrology, v. 33, n. 4, p. 785–815, http://dx.doi.org/10.1093/petrology/33.4.785

Watson, E. B., and Harrison, T. M., 1983, Zircon saturation revisited: Temperature and composition effects on a variety of crustal magma types: Earth Planetary Science Letters, v. 64, n. 2, p. 295–304, http://dx.doi.org/10.1016/0012-821X(83)90211-X

Watt, G. R., Burns, I. M., and Graham, G. A., 1996, Chemical characteristics of migmatites: Accessory phase distribution and evidence for fast melt segregation rates: Contributions to Mineralogy and Petrology, v. 125, n. 1, p. 100–111, http://dx.doi.org/10.1007/s004100050209

Westaway, R., 2006, Cenozoic cooling histories in the Menderes Massif, western Turkey, may be caused by erosion and flat subduction, not low-angle normal faulting: Tectonophysics, v. 412, n. 1–2, p. 1–25, http://dx.doi.org/10.1016/j.tecto.2005.08.005

Whitney, D. L., Teyssier, C., Toraman, E., Seaton, N. C. A., and Fayon, A. K., 2011, Metamorphic and tectonic evolution of a structurally continuous blueschist-to-Barrovian terrane, Sivrihisar Massif, Turkey: Journal of Metamorphic Geology, v. 29, n. 2, p. 193–212, http://dx.doi.org/10.1111/j.1525-1314.2010.00915.x

Wiedenbeck, M., Allé, P., Corfu, F., Griffin, W. L., Meier, M., Oberli, F., Von Quadt, A., Roddick, J. C., and Spiegel, W., 1995, Three natural zircon standards for U-Th-Pb, Lu-Hf, trace-element and REE analyses: Geostandards Newsletter, v. 19, n. 1, p. 1–23, http://dx.doi.org/10.1111/j.1751-908X.1995.tb00147.x

Williams, I. S., and Claesson, S., 1987, Isotopic evidence for the Precambrian provenance and Caledonian metamorphism of high grade paragneisses from the Seve Nappes, Scandinavian Caledonides: Contributions to Mineralogy and Petrology, v. 97, n. 2, p. 205–217, http://dx.doi.org/10.1007/BF00371240

Wilson, M., 1989, Igneous Petrogenesis; a global tectonic approach: London, Unwin Hyman, 466 p.